Photoproduction of π^0 mesons off protons and neutrons in the second and third nucleon resonance regions

M. Dieterle,[1] D. Werthmüller,[1,2] S. Abt,[1] F. Afzal,[3] P. Aguar Bartolome,[4] Z. Ahmed,[5] J. Ahrens,[4] J. R. M. Annand,[2] H. J. Arends,[4] M. Bashkanov,[6] R. Beck,[3] M. Biroth,[4] N. Borisov,[7] A. Braghieri,[8] W. J. Briscoe,[9] S. Cherepnya,[10] F. Cividini,[4] C. Collicott,[11] S. Costanza,[8,*] A. Denig,[4] E. J. Downie,[9] P. Drexler,[4,12] L. V. Fil'kov,[10] S. Garni,[1] D. I. Glazier,[2,6] I. Gorodnov,[7] W. Gradl,[4] M. Günther,[1] D. Gurevich,[13] L. Heijkenskjöld,[4] D. Hornidge,[14] G. M. Huber,[5] A. Käser,[1] V. L. Kashevarov,[4,7] S. Kay,[6] I. Keshelashvili,[1,†] R. Kondratiev,[13] M. Korolija,[15] B. Krusche,[1,‡] A. Lazarev,[7] V. Lisin,[13] K. Livingston,[2] S. Lutterer,[1] I. J. D. MacGregor,[2] D. M. Manley,[16] P. P. Martel,[4,17] J. C. McGeorge,[2] V. Metag,[12] D. G. Middleton,[17] R. Miskimen,[18] E. Mornacchi,[4] A. Mushkarenkov,[8,18] A. Neganov,[7] A. Neiser,[4] M. Oberle,[1] M. Ostrick,[4] P. B. Otte,[4] B. Oussena,[4,9] D. Paudyal,[5] P. Pedroni,[8] A. Polonski,[13] S. N. Prakhov,[19] G. Ron,[20] T. Rostomyan,[1,§] A. Sarty,[11] C. Sfienti,[4] V. Sokhoyan,[4] K. Spieker,[3] O. Steffen,[4] I. I. Strakovsky,[9] T. Strub,[1] I. Supek,[15] A. Thiel,[3] M. Thiel,[4] A. Thomas,[4] M. Unverzagt,[4] Yu. A. Usov,[7] S. Wagner,[4] N. K. Walford,[1] D. P. Watts,[6] J. Wettig,[4] L. Witthauer,[1] M. Wolfes,[4] and L. A. Zana[6]
(A2 Collaboration)

[1]*Department of Physics, University of Basel, Ch-4056 Basel, Switzerland*
[2]*SUPA School of Physics and Astronomy, University of Glasgow, Glasgow, G12 8QQ, United Kingdom*
[3]*Helmholtz-Institut für Strahlen- und Kernphysik, University Bonn, D-53115 Bonn, Germany*
[4]*Institut für Kernphysik, University of Mainz, D-55099 Mainz, Germany*
[5]*University of Regina, Regina, Saskatchewan S4S-0A2, Canada*
[6]*SUPA School of Physics, University of Edinburgh, Edinburgh EEH9 3JZ, United Kingdom*
[7]*Joint Institute for Nuclear Research, 141980 Dubna, Russia*
[8]*INFN Sezione di Pavia, I-27100 Pavia, Pavia, Italy*
[9]*Center for Nuclear Studies, The George Washington University, Washington, DC 20052, USA*
[10]*Lebedev Physical Institute, RU-119991 Moscow, Russia*
[11]*Department of Astronomy and Physics, Saint Mary's University, E4L1E6 Halifax, Canada*
[12]*II. Physikalisches Institut, University of Giessen, D-35392 Giessen, Germany*
[13]*Institute for Nuclear Research, RU-125047 Moscow, Russia*
[14]*Mount Allison University, Sackville, New Brunswick E4L1E6, Canada*
[15]*Rudjer Boskovic Institute, HR-10000 Zagreb, Croatia*
[16]*Kent State University, Kent, Ohio 44242, USA*
[17]*Mount Allison University, Sackville, New Brunswick E4L3B5, Canada*
[18]*University of Massachusetts, Amherst, Massachusetts 01003, USA*
[19]*University of California Los Angeles, Los Angeles, California 90095-1547, USA*
[20]*Racah Institute of Physics, Hebrew University of Jerusalem, Jerusalem 91904, Israel*

(Received 14 March 2018; published 21 June 2018)

Background: Photoproduction of mesons off quasifree nucleons bound in the deuteron allows us to study the electromagnetic excitation spectrum of the neutron and the isospin structure of the excitation of nucleon resonances. The database for such reactions is much more sparse than for free proton targets.

Purpose: Study experimentally single π^0 photoproduction off quasifree nucleons from the deuteron. Investigate nuclear effects by a comparison of the results for free protons and quasifree protons. Use the quasifree neutron data (corrected for nuclear effects) to test the predictions of reaction models and partial wave analysis (PWA) for $\gamma n \to n\pi^0$ derived from the analysis of the other isospin channels.

Methods: High statistics angular distributions and total cross sections for the photoproduction of π^0 mesons off the deuteron with coincident detection of recoil nucleons have been measured for the first time. The experiment was performed at the tagged photon beam of the Mainz Microtron (MAMI) accelerator for photon energies between 0.45 and 1.4 GeV, using an almost 4π electromagnetic calorimeter composed of the Crystal Ball and TAPS detectors. A complete kinematic reconstruction of the final state removed the effects of Fermi motion.

Results: Significant effects from final-state interactions (FSI) were observed for participant protons in comparison to free proton targets (between 30% and almost 40%). The data in coincidence with recoil neutrons were corrected for such effects under the assumption that they are identical for participant protons and neutrons. Reaction model predictions and PWA for $\gamma n \to n\pi^0$, based on fits to data for the other isospin channels, disagreed between themselves and no model provided a good description of the new data.

Conclusions: The results demonstrate clearly the importance of a measurement of the fully neutral final state for the isospin decomposition of the cross section. Model refits, for example from the Bonn-Gatchina analysis, show

that the new and the previous data for the other three isospin channels can be simultaneously described when the contributions of several partial waves are modified. The results are also relevant for the suppression of the higher resonance bumps in total photoabsorption on nuclei, which are not well understood.

DOI: 10.1103/PhysRevC.97.065205

I. INTRODUCTION

The photoproduction of mesons is a prime tool for the study of the excitation spectrum of the nucleon, which is a major testing ground for the properties of the strong interaction in the nonperturbative regime. The pion is the lightest meson and has a strong coupling to many nucleon excited states. Although recent years have provided new photoproduction data for many different final states, pion scattering and photoproduction of pions are still central to most analyses which aim to identify and characterize the excited states of nucleons. Many theoretical frameworks are employed to extract this information. They include the SAID multipole analysis [1,2], the MAID unitary isobar model [3,4], the Dubna-Mainz-Taipei (DMT) dynamical model [5], the Bonn-Gatchina (BnGa) coupled-channel analysis [6], the effective Lagrangian models of the Giessen group [7,8] and the Madrid group [9], the Jülich-Bonn dynamical coupled-channel analysis [10], the Kent State University (KSU) model [11], and the analysis of the recent CLAS data for the electroproduction of pions [12].

The database for pion photoproduction off the free proton is large and rapidly growing, in particular for the $\gamma p \to p\pi^0$ reaction [13–28] (references to data sets published before 2005 can be found in Ref. [15]), including results from the measurements of single and double polarization observables with CLAS at Jefferson Laboratory (JLab), Crystal Barrel/TAPS at ELSA, Crystal Ball/TAPS at MAMI, and GRAAL at European Synchrotron Radiation Facility (ESRF). However, a complete partial wave analysis (PWA) necessitates the isospin decomposition of the electromagnetic excitations [29]. This requires the measurement of at least one pion production reaction off the neutron. The database for meson production reactions off the neutron, in particular for neutral pions, is significantly sparser than the proton data. Historically, the difference arose because of the complications involved in measurements with quasifree neutrons. However, many efforts are currently under way to improve this situation [30].

The database for angular distributions of single pion production reactions off the nucleon which was available when the present results were published as a Letter [31] is summarized in Fig. 1. In the meantime, further data for the $\gamma n \to p\pi^-$ reaction have been published from the CLAS experiment [32,33]. The figure shows the kinematic ranges covered by the previous data, binned in invariant mass W and center of momentum (cm) angle $\theta_\pi^\star$ [plotted is $\cos(\theta_\pi^\star)$]. Also shown are the present data points for the $\gamma n \to n\pi^0$ reaction, which had previously only been minimally investigated. Data for polarization observables for the $n\pi^0$ final state were also very sparse until recently. The beam asymmetry Σ has been measured by the GRAAL Collaboration [34] and first results for the double polarization observable E measured with longitudinally polarized target and circularly polarized beam were reported by the Crystal Ball/TAPS Collaboration [35] very recently. In the range of the Δ resonance, results for the helicity dependence of single pion production were also reported from the GDH experiment at MAMI [36], but mainly for charged pions and at photon energies lower than those in the present experiment.

The situation is better for $\gamma n \to p\pi^-$ since this final state can be detected with magnetic spectrometers. One might argue that the lack of data for the $n\pi^0$ final state is not a severe problem, since in principle the measurement of the other three isospin channels (see below) is enough to fix the three independent isospin amplitudes A^{IS}, A^{IV}, and A^{V3} [29]. However, the predictions of different reaction models and PWA for $\gamma n \to n\pi^0$ based on the results of the other isospin channels differed widely [31]. The main problem is that for the isospin channels with charged pions, contributions from nonresonant backgrounds are much more important [29]. In the absence of complete data sets with a sufficient database of polarization observables [37], significant model dependencies can exist.

The photoproduction of neutral pions has the advantage that background contributions, e.g., from Kroll-Rudermann or pion-pole terms, are suppressed because the incident photon cannot couple to the pion via its charge. A simple example is pion photoproduction in the Δ-resonance region summarized in Fig. 2. It follows immediately from the isospin decomposition that for pure excitation of the P_{33} resonance, without background contributions, the cross sections for the four isospin channels are related by

$$\begin{aligned}\sigma(\gamma p \to p\pi^0) &= \sigma(\gamma n \to n\pi^0)\\ &= 2\sigma(\gamma p \to n\pi^+) = 2\sigma(\gamma n \to p\pi^-),\end{aligned} \tag{1}$$

which is obviously not the case for the experimental results. The reason is the large background contribution to the reactions with charged pions in the final state. The MAID model results for the P_{33} (dashed lines in the figure) respect this relation. However, roughly 50% of the cross section for the charged channels at the Δ peak position are related to background contributions, which are even different for the positively and negatively charged pions. Therefore, experimental data for the

*Also at Dipartimento di Fisica, Università di Pavia, I-27100 Pavia, Italy.

†Present adaress: Institut für Kernphysik, FZ Jülich, 52425 Jülich, Germany.

‡Corresponding author: bernd.krusche@unibas.ch

§Present address: Department of Physics and Astronomy, Rutgers University, Piscataway, New Jersey, 08854-8019, USA.

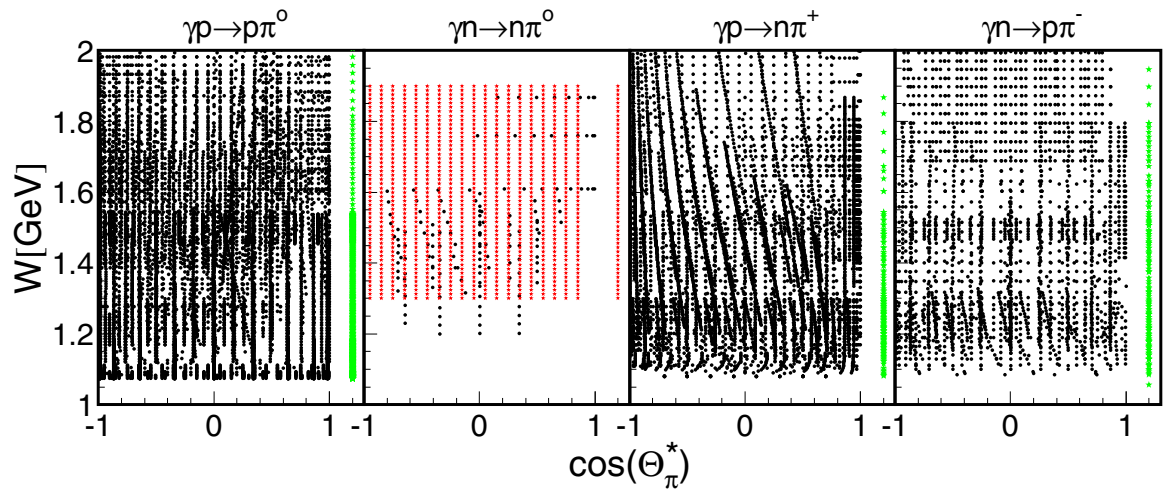

FIG. 1. Data coverage for angular distributions and total cross sections [green stars at $\cos(\theta_\pi^\star) = 1.1$] for the photoproduction of pions off the nucleon as a function of invariant mass W and of pion momentum polar angle $\theta_\pi^\star$. Black circles, previous data; red stars, $n\pi^0$ final-state results from this work.

$n\pi^0$ channel are necessary for better control of the separation of resonance and background contributions in the reaction models.

Measurements off quasifree neutrons are complicated by nuclear Fermi motion and possible nucleon-nucleon and nucleon-meson final-state interaction (FSI) effects. The effects from Fermi motion can be reliably removed (within experimental resolution) with a kinematic reconstruction of the final-state invariant mass [30]. Thus, they are not problematic unless narrow structures in the cross section must be resolved. The importance of FSI effects can vary considerably for different final states. This can be tested with a comparison of the cross-sectional data for free and quasifree protons. Results for quasifree photoproduction of η and η' mesons off the deuteron [42,43] show no significant FSI influence at the current level of statistical precision of the experimental data. However, results for the quasifree $\gamma n \to p\pi^-$ reaction [32,44–46] found significant FSI effects, in particular for forward-meson angles. This is the kinematic regime where nucleon-nucleon FSI becomes important because of the small relative momentum between the "participant" and "spectator" nucleons. Also, this complication makes it desirable to study both pion reaction channels off the quasifree neutron, which will allow better approximations of such systematic effects.

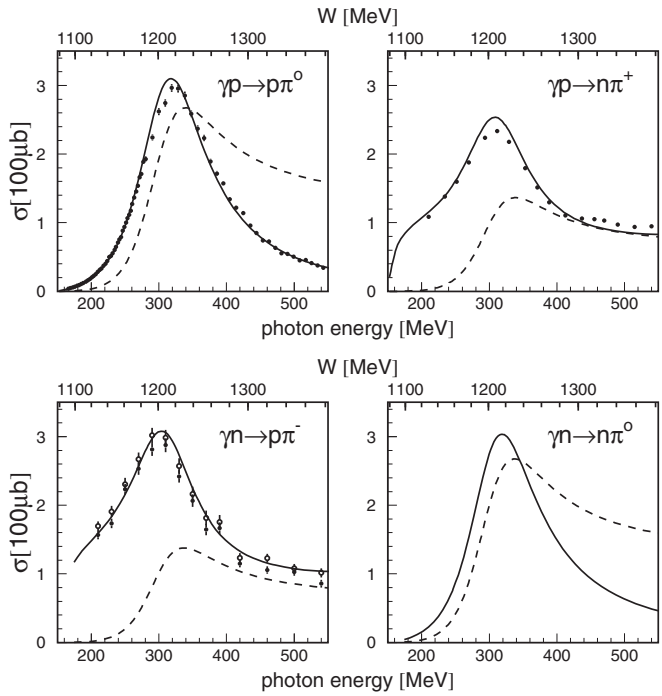

FIG. 2. Pion production in the Δ-resonance region. Measured cross sections: $p\pi^0$ final state [38,39], $n\pi^+$ final state [40], and $p\pi^-$ final state [41]. Curves, MAID model [3]; solid, full model; and dashed, only $P_{33}(1232)$ resonance.

In the case of π^0 photoproduction off the deuteron, the coherent process $\gamma d \to d\pi^0$ will contribute in addition to the breakup reaction $\gamma d \to np\pi^0$. This contribution is large in the Δ-resonance region, in particular for pion forward angles, and it removes strength from the quasifree reactions [39]. The net effect is that the sum of the elementary cross sections for free protons and free neutrons—after folding with Fermi motion—is better approximated by the inclusive cross section for $\gamma d \to X\pi^0$ than by the sum of the exclusive quasifree cross sections for $\gamma d \to p\pi^0(n)$ and $\gamma d \to n\pi^0(p)$. In the Δ-resonance region, such effects have been studied in detail with models taking into account FSI and with experimental data comparing free and quasifree production off protons [47,48]. The coherent contribution diminishes at higher incident photon energies, due to the deuteron form factor.

Prior to this experiment, to our knowledge, no data for the exclusive quasifree reactions $\gamma d \to (n)p\pi^0$, $\gamma d \to n(p)\pi^0$ (in parentheses: spectator nucleon) existed. There are, however, some results for the inclusive reaction $\gamma d \to X\pi^0$ [39]

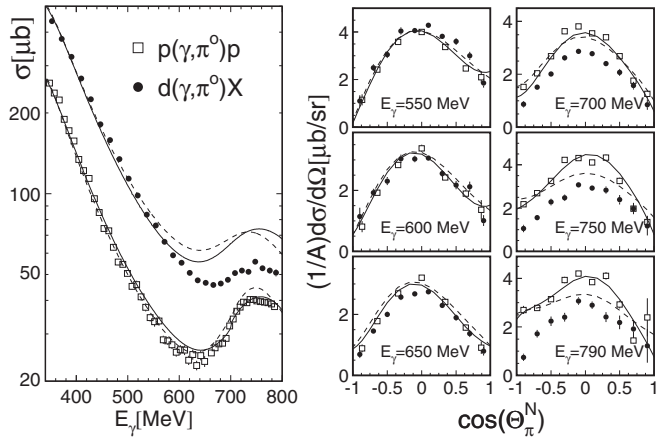

FIG. 3. Single π^0 photoproduction off the free proton and the deuteron in the second resonance region [note that $d(\gamma,\pi^0)X$ includes the $np\pi^0$ and $d\pi^0$ final states] [39]. Left-hand side: total cross sections. Curves: results from the SAID analysis [1] (solid) and MAID model [3] (dashed). For the deuteron from both models, the sum of proton and neutron cross sections folded with nuclear Fermi motion is plotted. Right-hand side: angular distributions. Solid curves, SAID proton, and dashed curves, Fermi smeared average of SAID proton and neutron.

up to the second resonance region (see Fig. 3). The second resonance peak is less prominent in these data than for free protons. The Fermi smeared sum of the results of the SAID [1] and MAID [3] models for the elementary reactions on protons and neutrons agreed with the measured cross section in the tail of the Δ resonance, but overestimated the second resonance peak. It was unclear whether this indicated a problem of the models for the neutron cross section, large FSI effects, or both. Only an exclusive measurement with coincident recoil nucleons could clarify this.

The present work summarizes the results from a measurement of single π^0 photoproduction off the deuteron with detection of the pion-decay photons and the recoil nucleons for incident photon energies from ≈450 to 1400 MeV. The paper is organized in the following way: A short description of the experimental setup is given in Sec. II. The different steps of the analysis are discussed in Sec. III. In Sec. IV, we first discuss the results for the quasifree processes as a function of incident photon energy (i.e., cross sections folded with nuclear Fermi motion) and subsequently the results as function of final-state invariant mass, which can be compared to previous experimental data for the proton target and to model predictions for the free cross sections for protons and neutrons. Some of the results have already been published in a Letter [31]. This paper gives more details about the analysis and presents also results which could not be included in the Letter (e.g., the experimental data without corrections for Fermi motion).

II. EXPERIMENTAL SETUP

The experiment was performed at the electron accelerator facility MAMI in Mainz [49–51] using a quasimonochromatic photon beam with energies between ≈0.45 and ≈1.4 GeV from the Glasgow tagged photon spectrometer [52–54]. In total, three beam times with a liquid deuterium target were taken (see Refs. [55–58] for details). One of them, optimized for multiple meson production, used a trigger with hit multiplicity three and was not analyzed for the present results. The two beam times analyzed here used primary electron beams with energies of 1.508 and 1.557 GeV, which produced bremsstrahlung in a copper radiator of 10 μm thickness. The typical energy resolution of the photon beam was defined by the 4-MeV bin width of the tagger focal plane detectors. The electron beam was longitudinally polarized so that the photon beam was circularly polarized. This was, however, irrelevant for the present results since the target was unpolarized and single-meson production from an unpolarized target shows no asymmetries for a circularly polarized beam due to parity conservation. The polarization degree of freedom was used in the analysis of the production of meson pairs ($\pi^0\pi^{0,\pm}$, $\pi^{0,\pm}\eta$), which were measured simultaneously [56,58,59].

The target material was liquid deuterium contained in Kapton cylinders of ≈4 cm diameter and 4.72 or 3.02 cm length corresponding to surface densities of 0.231 nuclei/b or 0.147 nuclei/b, respectively. The beam spot size on the target (≈1.3 cm diameter) was defined by a collimator (4 mm diameter) placed downstream from the radiator foil. The photon flux, needed for the absolute normalization of the cross sections, was derived from the number of deflected electrons and the fraction of correlated photons that pass the collimator and reach the target (tagging efficiency). The flux of scattered electrons was counted by live-time-gated scalers. The tagging efficiency was determined with special experimental runs. A total absorbing lead-glass counter was moved into the photon beam at reduced intensity of the primary electron beam. In addition to these periodical absolute measurements, the photon beam intensity was monitored in arbitrary units during normal data collection with an ionization chamber at the end of the photon-beam line.

Photons and recoil nucleons were detected using an almost 4π electromagnetic calorimeter, supplemented with detectors for charged particle identification (see Fig. 4). More details of the calorimeter (in a slightly different configuration) are given in Refs. [60,61]. The setup combined the Crystal Ball (CB) detector [62] with a hexagonal forward wall constructed from 384 BaF_2 modules from the TAPS array [63,64]. Between the two beam times, TAPS was modified by replacing the two innermost rings close to the beam pipe by trapezoidally shaped $PbWO_4$ crystals (four crystals for each BaF_2 module) to increase rate capability. However, these new modules were not yet operational and were not used in the analysis. The Crystal Ball is made of 672 NaI detectors, arranged in two half spheres, which together cover the full azimuthal range for polar angles from 20° to 160°, corresponding to 93% of the full solid angle. The TAPS forward wall was placed 1.468 m downstream from the target and covered polar angles between ≈5° and 21°. All TAPS modules were equipped with individual plastic scintillators (Charged Particle Veto, CPV) in front of the crystals for charged particle identification. The target cell with the liquid deuterium was mounted from the upstream side with its cryosupport structures in the center of the CB. It was surrounded by a detector for charged particle identification

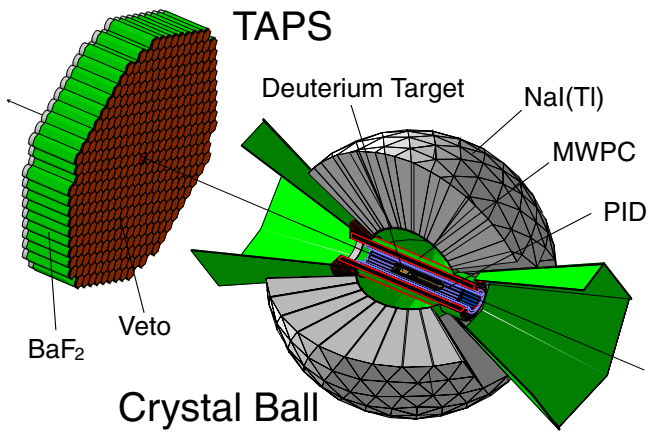

FIG. 4. Setup of the electromagnetic calorimeter combining the Crystal Ball and TAPS (left-hand-side) detectors. Only three quarters of the Crystal Ball are shown. Detectors for charged particle identification were mounted in the Crystal Ball (PID and MWPC) and in front of the TAPS forward wall (TAPS Veto-detector, CPV). The beam enters from the bottom right corner of the figure.

(PID) [65] and multiwire-proportional chambers (MWPC), which were fitted into the beam tunnel of the CB. The MWPC for charged particle tracking were not used in the present analysis. The PID consisted of 24 plastic scintillators, which surrounded the target and provided full azimuthal coverage. Each scintillator covered 15° of azimuthal angle and the same range in polar angle as the CB, i.e., from 20° to 160°. The PID did not provide polar angle information.

For trigger purposes, the CB and TAPS were subdivided into logical sectors. The CB was split into 45 rectangular areas (after projecting its geometry on a plane) and TAPS into 6×64 modules in a pizza-slice geometry. The trigger condition used for the present analysis was a multiplicity of two logical sectors with the signal of at least one detector module above a threshold of about 30 MeV (CB) or 35 MeV (TAPS) and the analog energy-sum signal from the CB above 300 MeV. This condition was not optimized for the measurement of single π^0 production, but for the simultaneous measurement of η and multiple meson production reactions. Events with both photons going into TAPS were not accepted. In the analysis, only events were used for which these conditions were fulfilled already by the π^0-decay photons. Events where the trigger was only activated due to the additional energy deposition of the recoil nucleon were discarded in order to avoid systematic uncertainties (the energy response of the detector was calibrated for photon showers, not for recoil nucleons). For accepted events, the readout thresholds for the detector modules were set to 2 MeV for the CB crystals, to 3–4 MeV for the TAPS crystals, to 250 keV for the TAPS charged-particle scintillators, and to 350 keV for the elements of the PID.

III. DATA ANALYSIS

The data used for the present analysis were also used to investigate several other meson production reactions (η mesons [57,66], $\pi\pi$ pairs [55,56,59], and $\pi\eta$ pairs [58,67]). The reliability of the raw data, of the calibration procedures, and of the analysis strategies was tested in several independent ways and details have been given in the above-mentioned publications. Therefore, only a summary of the main analysis steps and specific details for the analysis of the $\gamma N \to N\pi^0$ reactions with quasifree nucleons are given here.

The analysis was based on five main steps: (1) the calibration of all detector elements in use (Crystal Ball, TAPS, PID, CPV, and tagging spectrometer) in view of energy and/or timing information, (2) the identification of events from the $\gamma N \to N\pi^0$ reaction (particle identification, invariant, and missing mass analyses, etc.), (3) the absolute normalization of the cross sections (beam flux, target density, and Monte Carlo simulations of the detection efficiency), (4) the reconstruction of the total cm energy W from the final-state kinematics for events in which the effects of Fermi motion were removed, and (5) the correction for FSI for the quasifree neutron results.

A. Detector calibration

A detailed description of the detector performance and the calibration procedures was already given in Refs. [57,58,60,61,68]. Timing information was available for the plastic scintillators of the focal plane (FP) detector of the tagging spectrometer, the NaI crystals of the CB, the BaF_2 modules of TAPS, the plastic scintillators of the PID detector, and the scintillators from the TAPS veto detector. The CB and the FP detector were equipped with CATCH TDCs of a fixed conversion gain of 117 ps/channel. The gains of the TAPS modules were calibrated by inserting delay cables of precisely known lengths into the common stop signal. The offsets (time zero position of the signals) were calibrated by iterative procedures comparing coincident signals within and between different detector components. The slow signals from the CB detector, analyzed with leading edge discriminators (LED), required in addition an energy-dependent time-walk correction, which greatly improved time resolution. In contrast, the fast signals from the TAPS detector analyzed with constant fraction discriminators (CFD) needed no time-walk correction. Typical time resolutions (time spectra are, e.g., shown in Refs. [57,68]) with this setup are listed in Table I.

Most important were the CB-Tagger and TAPS-Tagger time resolutions because the size of the background from random tagger and production-detector coincidences depends on it. The random background was removed in the usual

TABLE I. Typical time resolutions (FWHM) for coincidences between different detector components.

Detector coincidence	Typical resolution [ns]
TAPS-TAPS	0.45–0.55
TAPS-CB	1.3–1.0
CB-CB	2.0–3.0
TAPS-Tagger	0.8–1.0
CB-Tagger	1.4–1.6

way by a sideband subtraction in the time spectra (see, e.g., Refs. [57,68]). Furthermore, the timing information from the TAPS detector was important for a time-of-flight (ToF) versus energy analysis for the separation of different particle types in the TAPS forward detector. The CB-CB timing information and the timing informations from the PID and TAPS CPV were only used to assure that hits in these detectors corresponded to the same event. However, the background from event overlap was anyway negligible, so that time resolution was not an important issue in this case. Energy information was available from the modules of the CB and TAPS calorimeters and the PID and TAPS CPV devices. For the photon tagger, energy information came not from the response of the FP scintillators but from their geometric position in the focal plane calibrated by special measurements [54] with direct deflection of electron beams of precisely known energies into the focal plane.

The primary pre-data-collection calibration of TAPS was done with cosmic muons, which (as minimum ionizing particles) deposit on average approximately 37.7 MeV per crystal because, in contrast to the CB, all crystals have the same geometry and are horizontally oriented in the same way. A rough energy calibration of the CB was done before data collection with an ^{241}Am/^{9}Be source (photons of 4.438 MeV and a continuous neutron spectrum up to about 10 MeV) placed at the target position.

The final calorimeter calibration started with the CB. In an iterative procedure, the invariant mass of photon pairs identified as decay products of π^0 mesons was first used for a linear calibration. This was subsequently improved by a quadratic term derived from the invariant mass of photon pairs from η-meson decays. The energy response of the TAPS detector was calibrated in the same way. However, since two-photon hits in TAPS are rare for π^0 decays and almost impossible for η decays, events with one photon in CB and one photon in TAPS had to be used. Therefore, the TAPS calibration depends on the previous CB calibration. Furthermore, the scintillation light from BaF_2 crystals has two different components with different wavelengths, decay times, and relative intensities depending on the type of the detected particle [63,64]. This feature is routinely exploited by a pulse-shape analysis (PSA) used for particle identification by integrating the signals over short and long gate periods. Therefore, two independent energy signals had to be calibrated for TAPS. As usual, the calibration was done in a way that the calibrated short-gate and long-gate energy signals were identical for photons.

The energy response of the PID detector was calibrated by a comparison of the $E - \Delta E$ spectra measured for clearly identified protons to the results from Monte Carlo simulations. The energy signals of the CPV were not further used in the analysis; their calibration was only relevant for the determination of the correct veto thresholds. This was also done by comparison to Monte Carlo simulations.

B. Particle identification

All results shown in this section were integrated over the full tagged and analyzed energy range of E_γ from 0.45 to 1.4 GeV. In the first step of the analysis, all modules of the main detectors CB and TAPS that detected a signal were grouped into connected clusters corresponding to hits from photons or massive particles in the calorimeter. The position, time, and energy information of the clusters were then derived by summing up or averaging over the signals from the activated crystals [60,64]. The position (i.e., the polar angle information) from clusters in the TAPS forward wall had to be corrected for the geometrical effect arising because the crystals arranged in a horizontal position were not pointing directly toward the target. This is a straightforward analytical correction, which only requires knowledge about the (energy-dependent) average depths of the energy deposition in the detector. Subsequently, the clusters were assigned to the two types, neutral or charged, depending, for the CB, on the response of the PID and, for TAPS, on the response of the CPV. For the CB, hits were assigned as charged when the PID registered a coincident hit between the central CB-cluster module and the PID-scintillator bar within an azimuthal angle of 15°. For TAPS, a hit was assigned as charged when the CPV element in front of the central cluster module or a CPV neighbor module of the central cluster module responded. Because of the horizontal arrangement of the TAPS modules, especially at larger polar angles, a charged particle may not pass the central CPV but pass the neighboring module at a different polar angle.

Three different types of events were analyzed for the present work. Events with exactly two neutral hits and one charged hit were accepted as candidates for the exclusive $\gamma d \to (n)p\pi^0$ reaction (σ_p, π^0, and participant proton). Events with exactly three neutral hits were analyzed for the exclusive $\gamma d \to (p)n\pi^0$ reaction (σ_n, π^0, and participant neutron). "Participant" proton (or neutron) were assigned as the nucleon detected in coincidence with the pion. In rare cases, due to Fermi momenta in the tail of the bound-nucleon momentum distribution, also detection of the "spectator" nucleon was possible. This was included into the Monte Carlo (MC) simulations of detection efficiency; only second-order effects from FSI modifying the tail of the distributions could not be accounted for. In addition, the inclusive reaction $\gamma d \to X\pi^0$ (σ_{incl}) was analyzed, where X corresponded to a charged, a neutral, or no third hit in the calorimeter. This sample included events for which the recoil nucleon was not detected (if it was detected, it was ignored in the analysis) and also events from the $\gamma d \to d\pi^0$ reaction. This inclusive analysis was independent of recoil nucleon detection efficiencies.

For all events with three neutral hits, the most probable assignment of them to the two π^0-decay photons and a neutron candidate was determined by a χ^2 test for which the invariant masses of all pairs of neutral hits were compared to the nominal mass m_{π^0} of the π^0 meson

$$\chi^2(\gamma_i,\gamma_j) = \left(\frac{m_{\gamma_i,\gamma_j} - m_{\pi^0}}{\Delta m_{\gamma_i,\gamma_j}}\right)^2, \tag{2}$$

where m_{γ_i,γ_j} is the invariant mass of neutral hits i and j, $1 \leqslant i$, $j \leqslant 3$, $i \neq j$, and $\Delta m_{\gamma_i,\gamma_j}$ is their uncertainty computed from the experimental energy and angular resolution (determined with MC simulations). Only the best combination was kept for further analysis. This applied to the events analyzed for σ_n and the subset of events for σ_{incl} with three neutral hits.

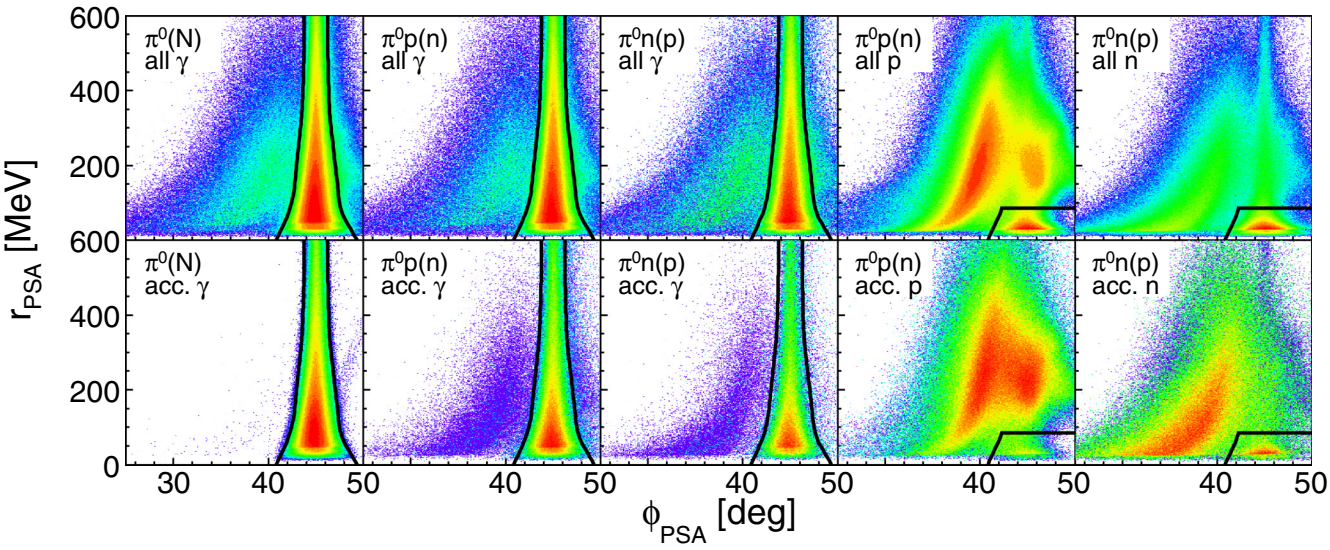

FIG. 5. PSA spectra for hits in TAPS. Top row: raw spectra selected with information from CPV detector and χ^2 analysis (where applicable). From left to right: photon candidates for inclusive analysis (no condition for recoil nucleons), photons with coincident proton candidates, photons with coincident neutron candidates, candidates for recoil protons, and candidates for recoil neutrons. Bottom row: same after application of all kinematic cuts. The black lines show the cuts applied to the spectra.

Further methods of particle-type identification were available for the TAPS forward wall, where they were important to distinguish recoil nucleons (which were mostly detected in the angular range covered by TAPS) from photon showers. A very efficient particle identification in TAPS was based on the PSA of the signals from the BaF_2 crystals. The scintillation light from BaF_2 crystals is composed of two components with different wave lengths and different decay constants, $\tau = 0.9$ ns for the "fast" component and $\tau = 650$ ns for the "slow" component. The relative intensity of the two components is different for electromagnetic showers induced by photons (or electrons) and stopped massive particles such as recoil protons and neutrons. Therefore, the signals were integrated over two ranges (short gate, 40 ns; long gate, 2 μs). The first integral added the fast component and a small fraction of the slow component and the second contained the total signal. Both signals were calibrated for photon energies, so that the short (E_s) and long gate (E_l) signals for photon hits were equal. For massive particles, E_s is then smaller than E_l. Instead of comparing E_s and E_l, it is more convenient to use a transformation to the PSA radius r_{PSA} and the PSA angle ϕ_{PSA} defined by

$$r_{\mathrm{PSA}} = \sqrt{E_s^2 + E_l^2} \quad \text{and} \quad \phi_{\mathrm{PSA}} = \arctan(E_s/E_l). \qquad (3)$$

In this representation, photon hits appear at $\phi_{\mathrm{PSA}} \approx 45^\circ$ independent of r_{PSA} and recoil nucleons are located at smaller angles. Figure 5 summarizes typical PSA spectra. In the upper row, raw spectra are shown, for which hits have only been characterized as photons, protons, or neutrons by the response of the CPV and the χ^2 analysis of events with three neutral hits. The photon candidates are shown separately for reactions with no condition for recoil nucleons and for coincident protons and neutrons. The bottom row of the figure shows the same spectra after the application of the subsequent kinematic cuts (see Sec. III D). The photon sample was already quite clean for the raw data and application of the kinematic cuts removed most of the background. For the final analysis, an energy-dependent 3σ cut, indicated in the figure, was applied to these spectra. For the recoil nucleons, some background from abundant electromagnetic processes survived all other cuts (visible at $\approx$45° and small r_{PSA}) and was cut away in the PSA spectra. The spectrum for recoil neutrons was cleaned by the subsequent kinematic cuts, which removed events with three neutral hits for which the χ^2 assignment to photon and neutron hits was incorrect. The spectrum for recoil protons showed also in the region of expected photon hits ($\Phi_{\mathrm{PSA}} \approx 45^\circ$, r_{PSA} between 200 and 350 MeV) a significant structure. However, this is not background, but due to high-energy protons which were not stopped in TAPS, but punched through the detector (protons can be stopped in TAPS only up to kinetic energies of $\approx$400 MeV). The difference in the shape of the BaF_2 signals for heavy charged particles compared to electromagnetic showers is due to the depletion of electronic bands in the scintillator material close to the endpoint of the tracks of such particles. Therefore, punch-through protons not stopping in the scintillator produce signal shapes similar to photons. This effect is less pronounced for recoil neutrons, which, when not stopped by nuclear reactions, are usually not detected at all.

Further particle identification methods were based on $E - \Delta E$ analyses comparing the energy loss of charged particles in the PID (CPV) detectors to the total deposited energy in the CB (TAPS). The final result of the $E - \Delta E$ analysis for the CB-PID system is shown in Fig. 6. This spectrum shows a clean, background-free signal for recoil protons. Signatures for charged pions and deuterons were only visible in the raw spectra (not shown here; see, e.g., Ref. [56]) before application of the other cuts. The resolution for the corresponding analysis using the CPV-TAPS system was less good because, due to the readout with thin scintillating fibers, the light output from the

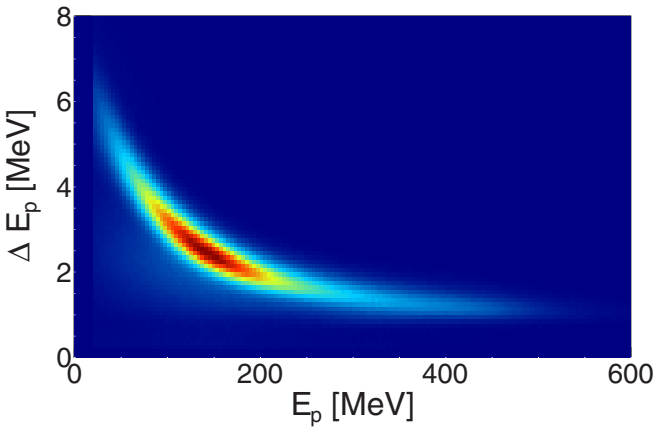

FIG. 6. Proton identification by the CB-PID detector system. Shown is the energy loss ΔE_p in the PID vs the total deposited energy E_p in the CB for hits identified as protons, after all other analysis cuts. No background from electrons or charged pions is visible.

CPV was low so that the energy resolution was worse than for the PID. Typical spectra for the same data set but from an analysis of the $\eta \to 2\gamma$ and the $\eta \to 3\pi^0 \to 6\gamma$ decays are shown in Ref. [57]. That analysis was not used here.

Because of the good time resolution of the TAPS detector and the relatively long flight path between the target and detector (≈1.5 m), the comparison of the time of flight to the total deposited energy was also a powerful method to assign hits in TAPS to different particle types. Spectra for proton and neutron candidates for two different angular ranges of the pions are shown in Fig. 7. Protons should appear in a relatively sharp band given by the relativistic velocity-energy relation. This was more or less the case for protons coincident with pions going to forward angles, which correspond to low proton laboratory energies. However, a small back-bending structure was visible already for this sample, corresponding to punch-through protons which did not deposit their full

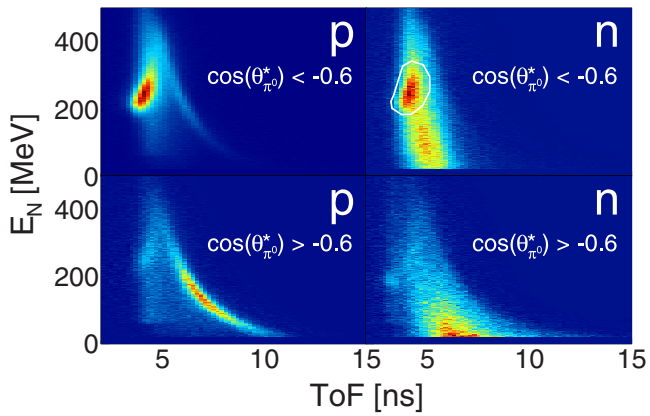

FIG. 7. Nucleon identification with the TAPS detector showing the deposited energy of the nucleon E_N vs its ToF (normalized to 1 m flight distance). Left column, proton; right column, neutron; top row, $\cos(\theta^*_{\pi^0}) < -0.6$; bottom row, $\cos(\theta^*_{\pi^0}) > -0.6$. The white line in the upper right histogram indicates background events from misidentified punch-through protons.

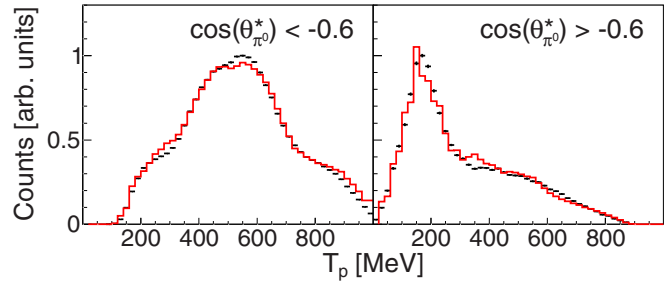

FIG. 8. Kinetic energy distribution of the recoil proton for exclusive single π^0 photoproduction off quasifree protons for two different regions of $\cos(\theta^*_{\pi^0})$. Black dots with error bars: Measured data, red line: MC signal.

energy in TAPS. This structure was much more pronounced for pions at backward angles, for which a large number of protons were high-energy, minimum-ionizing particles. No cuts were applied to the proton spectra. Typical kinetic energy distributions (from kinematic reconstruction of the events) of the protons corresponding to the two different ranges of pion-cm angles are shown in Fig. 8. Experimental results are compared to the output of the Monte Carlo simulations discussed in Subsec. III C.

With one exception discussed below, it was not necessary to apply cuts to the corresponding spectra. The background level in these spectra was already very low after the neutral/charged selection with the PID and CPV, the TAPS PSA cuts, the χ^2 analysis, and the kinematic cuts discussed in Subsec. III D.

Recoil neutrons can deposit any fraction of their kinetic energy in the detector and their signals are distributed over a large area in the ToF-versus-energy spectra. The neutron spectrum coincident with pions at $\cos(\theta^\star_{\pi^0}) > -0.6$ in Fig. 7 shows the expected behavior without any residual trace from the proton band, which would indicate misidentified protons. The neutron spectrum coincident with pions at $\cos(\theta^\star_{\pi^0}) < -0.6$ is less clean. It shows a significant structure from high-energy, minimum-ionizing protons which escaped detection from the CPV. The cut indicated by the white line in the figure was applied to remove this background. This cut was also applied to the data from the MC simulations for the detection efficiency (see Subsec. III C).

After this cut, the PSA spectra for protons and neutrons were inspected again for the two ranges of pion polar angles. The result is summarized in Fig. 9. The contribution of punch-through protons for backward pion angles is visible. For smaller pion angles, some intensity at PSA angles >45° from punch-through protons is also visible. The cut on ToF-versus-energy removed most background in this region in the neutron spectra. The only cuts applied to these spectra were as indicated in Fig. 5 (i.e., in the extreme lower right corners of the spectra).

For the separation of photon and neutron hits in the CB, only the χ^2 method could be used. Independent checks can be done with the analysis of the cluster multiplicity (i.e., the average number of activated crystals per hit in the detector), which is smaller for neutrons than for photons. This has been tested with the same data set for the analysis of η

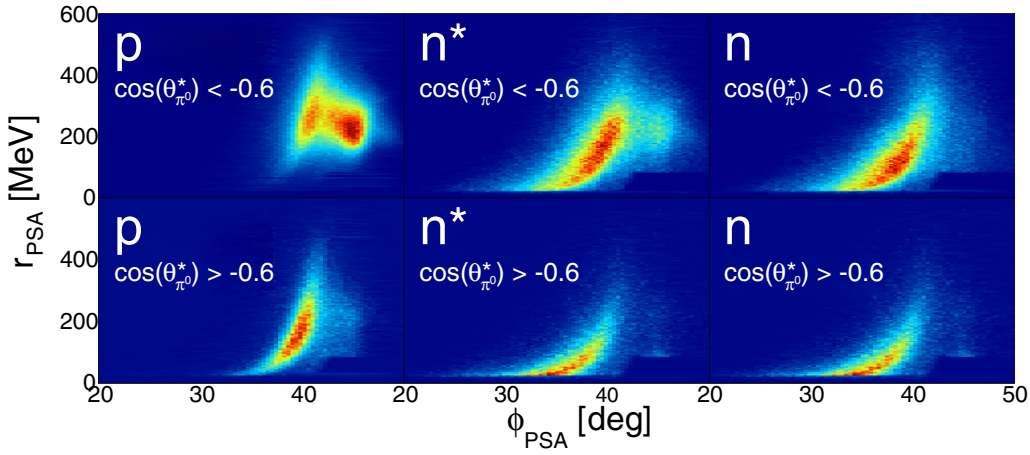

FIG. 9. PSA analysis of hits in the TAPS detector for nucleon candidates for events with forward and backward pion angles. Plotted is the PSA radius (r_{PSA}) vs the PSA angle (ϕ_{PSA}). Left column, proton; center column, neutron without ToF-versus-energy cut; right column, neutron with ToF-versus-energy cut. Top row, $\cos(\theta^*_{\pi^0}) < -0.6$; bottom row, $\cos(\theta^*_{\pi^0}) > -0.6$.

decays into two and six photons [57]. No indication for a significant cross contamination was found, but the method does not allow a stringent separation on an event-by-event basis, unless one accepts a large reduction of the statistical quality of the data by only accepting multiplicity-one hits as neutrons. No cuts were applied to cluster multiplicity in the present analysis.

C. Monte Carlo simulations

A reliable MC simulation of the response of the detector to the signal events is crucial for the absolute normalization of the experimental data. However, a comparison of signal and background events filtered through the detector response is also needed for the selection of the most efficient cuts for the identification of the reaction of interest. Therefore, the basic features of the MC simulations are discussed before details of the kinematic cuts applied to the data are given.

The MC simulations were based on the GEANT4 package [69]. All details of the detector setup, i.e., active components and inactive materials, were implemented as precisely as known. The quality of these simulations was already tested for other reactions analyzed from the same data set (see Refs. [55–58] for quasifree production of η mesons, pion pairs, and $\pi\eta$ pairs from deuterium) and also for beam-time periods with other targets (see Refs. [60,61,68] for hydrogen and ^{3}He targets). These analyses showed that the detector response to photon showers was correctly reproduced. Stringent tests came from the comparison of the results for η photoproduction using the $\eta \to 2\gamma$ and $\eta \to 3\pi^0 \to 6\gamma$ decays [57,68]. The results were in excellent agreement. Since even small inaccuracies in photon detection efficiency would lead to significant discrepancies, this indicates that the photon detection efficiency is well understood. The simulation of the response to recoil nucleons was more involved. The GEANT4 package offers several different physics models for the strong interaction of particles with matter [70]. Results from simulations using these different models were tested against the experimental data (e.g., the cluster size distributions of proton and neutron hits). For protons, not much variation was found between the different models. For neutrons, the best agreement was achieved when the BERTini cascade model and the high-precision (HP) neutron model [70] were included.

Results from the full simulation based on this model, including the electromagnetic showers of the photons and the recoil nucleons, are compared for several measured kinematic quantities in the next section. However, such simulations were not precise enough for the construction of the detection efficiency. Corrections derived from experimental data were necessary for the recoil nucleons. In particular, in the angular transition region from the CB to TAPS, inactive materials from support structures are complex and were not included with sufficient accuracy in the simulations. However, these are corrections which matter only for the exact values of absolute detection efficiencies for specific event topologies, but not for the discussion of the kinematic cuts in the next subsection. More details of the corrections required for the absolute normalization of cross sections are given in Sec. III F.

The input to the MC simulations was produced with event generators, which randomly generate events of the reactions of interest according to their kinematic characteristics. As a basis, the event generator PLUTO [71] was used, which was originally developed for heavy ion reactions. It had to be extended in two respects. The original version used incident particle beams of fixed energy. This was modified to an incident photon beam with a typical bremsstrahlung energy spectrum. It was also not designed to describe reactions with nucleons bound in nuclei, so that the effects from nuclear Fermi smearing had to be implemented. The parametrization of the deuteron wave function in momentum space from the Paris potential [72] was used. The simulated data were then analyzed with the same software package as the measured data.

It is not sufficient to simulate only the reaction of interest. The most important background reactions must also be simulated to optimize the cuts which discriminate against them. Removal of background from other reactions with the same final state, i.e., production of other mesons which decay to

photon pairs, can be easily removed by an invariant mass analysis of the photon pairs. More critical are backgrounds from reactions with additional particles that have escaped detection. For single π^0 production on the proton, $\gamma p \to \pi^0 p$, the following background contributions have been studied:

$$\begin{aligned}
&\gamma n \to \pi^0\pi^- p,\\
&\gamma n \to \Delta^+\pi^- \to \pi^0\pi^- p,\\
&\gamma p \to \pi^0\pi^0 p,\\
&\gamma p \to \pi^+\pi^-\pi^0 p, \quad \to \eta p \to \pi^+\pi^-\pi^0 p.
\end{aligned} \tag{4}$$

Similarly, for π^0 production on the neutron, $\gamma n \to \pi^0 n$, background from

$$\begin{aligned}
&\gamma p \to \pi^0\pi^+ n,\\
&\gamma p \to \Delta^+\pi^0 \to \pi^0\pi^+ n, \quad \to \Delta^0\pi^+ \to \pi^0\pi^+ n,\\
&\gamma n \to \pi^0\pi^0 n,\\
&\gamma n \to \pi^+\pi^-\pi^0 n, \quad \to \eta n \to \pi^+\pi^-\pi^0 n
\end{aligned} \tag{5}$$

was considered. For reactions where no intermediate state is given, phase-space distributions were used. The $\Delta\pi$ intermediate state was explicitly included for the production of pion pairs. In the energy range of interest, a significant fraction of such reactions is due to sequential resonance decays of the type $R \to \Delta\pi \to \pi\pi N$ (R: any higher lying resonance) or, even more important for charged pions, to the vertex $\gamma N \to \Delta\pi$ (Δ pion-pole or Δ Kroll-Rudermann-like diagrams) [55,61]. However, the contribution from $\Delta^0\pi^0$ intermediate states is negligible.

All reactions were simulated for incident nucleons bound in the deuteron. The dominant background was related to the final states $\pi^0\pi^+ n$ and $\pi^0\pi^- p$ where the charged pion had escaped detection because it was emitted in the direction of the beam pipe or too low in energy.

D. Reaction identification

With the analysis steps discussed above, hits in the two calorimeters were tentatively assigned to photons, recoil protons, and recoil neutrons. Only events with exactly two photon candidates (subsample for σ_{incl}) and events with exactly two photons and a proton or a neutron candidate were kept for further analysis. These events were then tested for their kinematic characteristics to identify single π^0 production. For all kinematic observables, the measured data were compared to the results of the MC simulations in order to test the quality of the simulations and to estimate the size of background contributions.

In the first step, the coplanarity of the events was analyzed. Neglecting the Fermi motion of the bound nucleons, there is no transverse momentum in the initial state. Consequently, due to momentum conservation, the reaction products, i.e., π^0 meson and recoil nucleon, must lie in one plane in the laboratory system. The difference $\Delta\Phi$ in azimuthal angle between the pion and the recoil nucleon must therefore be 180°. If a further, undetected meson was emitted, it should deviate from this value. Because of the Fermi motion of the bound nucleons and the angular resolution of the detector system, this relation is broadened around the ideal value.

This analysis was only possible for the exclusive reactions σ_p and σ_n, but not for σ_{incl}, which included events without detected recoil nucleons. The results are shown in Fig. 10. The experimental data were fitted with the line shapes of the simulated signal and background events. The background level was not high, but some components peaked at the position of the signal peak (although with a larger width which, in principle, would allow separation by a fit to these spectra). The background components were mainly due to undetected charged pions at extreme forward angles or small kinetic energies which did not contribute much to the transverse

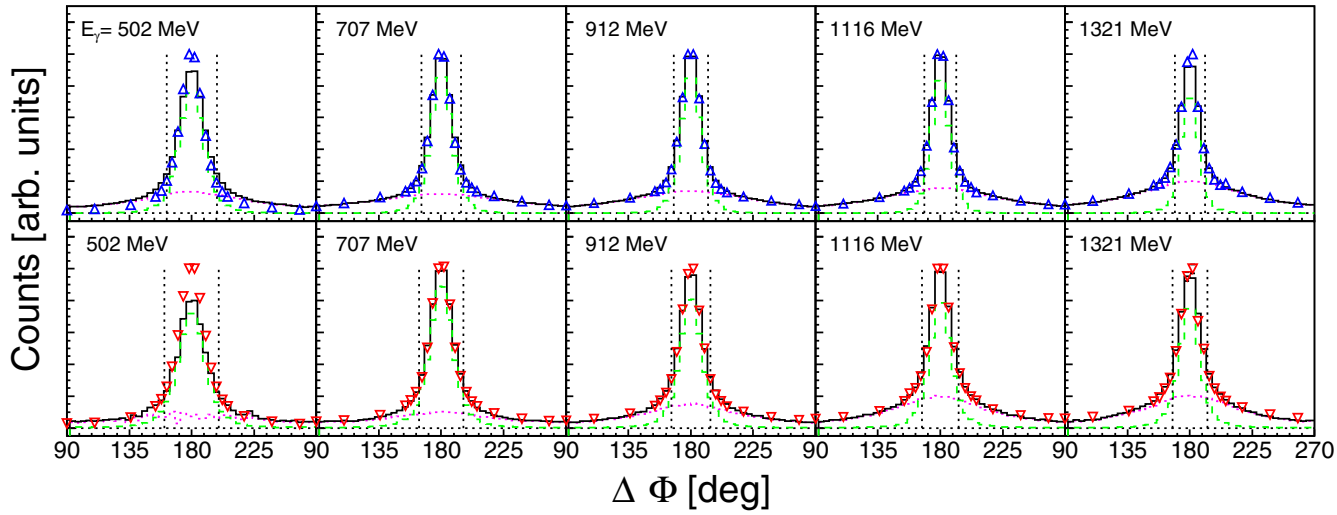

FIG. 10. Coplanarity angle distributions for several incident photon energies for exclusive single π^0 photoproduction off the quasifree proton (top, open upward blue triangles) and the quasifree neutron (bottom, open downward red triangles) integrated over the full angular range. Dashed green line, MC signal; dotted magenta line, sum of MC background contributions; solid black line, sum of MC signal and MC background; and dotted vertical lines, $\pm 1.5\sigma$ cut positions. Spectra shown have cuts on PSA, a rough invariant mass cut, and a χ^2 analysis for identification of recoil neutrons in CB.

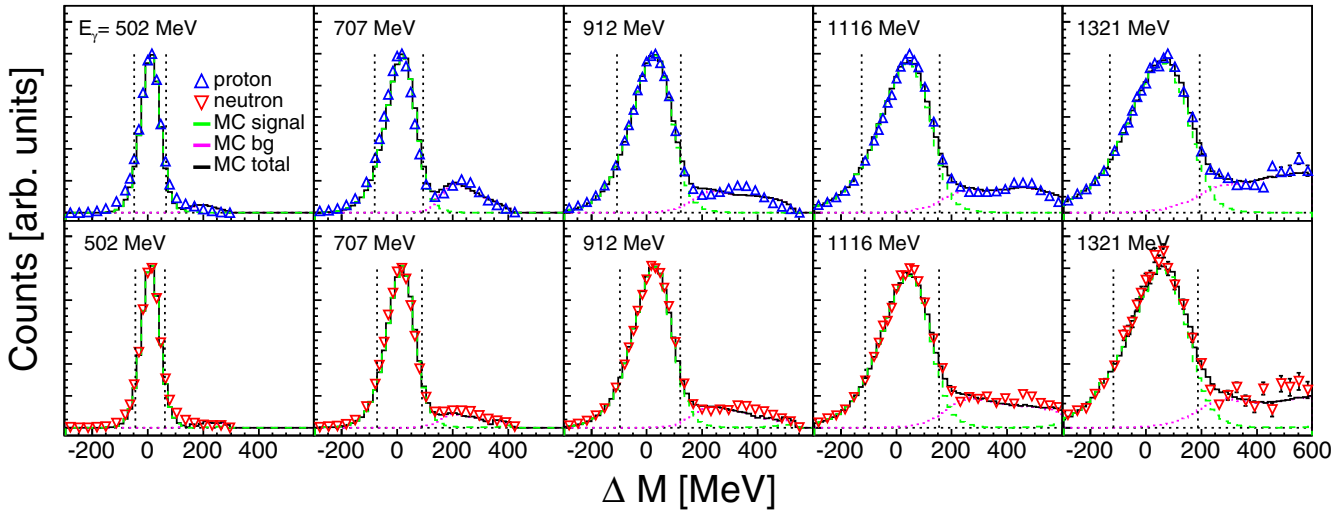

FIG. 11. Missing mass distributions for several incident photon energies for exclusive single π^0 photoproduction off the quasifree proton (top, open upward blue triangles) and the quasifree neutron (bottom, open downward red triangles) integrated over the full angular range. Dashed green line, MC signal; dotted magenta line, sum of MC background contributions; solid black line, sum of MC signal and MC background; and dotted vertical lines, $\pm 1.5\sigma$ cut positions. Spectra with cuts as indicated in Fig. 10 and additionally cuts on coplanarity as indicated in Fig. 10.

momentum balance. Such background is better removed by the missing mass analysis discussed below. For further analysis, only events within $\pm 1.5\sigma$ of the peak position were accepted (determined by Gaussian fits). In Fig. 10, five examples of these spectra integrated over the cm-polar angle are shown. However, the actual analysis and determination of the cuts was dependent on incident photon energy and cm-polar angle. The good agreement between the measured data and the results of the MC simulations demonstrates that the detector response and the effects of nuclear Fermi smearing were well under control.

For the following missing mass analysis, the recoil nucleons, if detected or not, were treated as missing particles and their mass was reconstructed from energy-momentum conservation under the hypothesis of single π^0 production from

$$\Delta M = |\mathbf{P}_\gamma + \mathbf{P}_N - \mathbf{P}_{\pi^0}| - m_N, \tag{6}$$

where $\mathbf{P}_\gamma$, $\mathbf{P}_N$, and $\mathbf{P}_{\pi^0}$ are the four-momenta of the incident photon, the incident nucleon (neglecting Fermi motion), and the final-state pion, respectively. The mass m_N of the participant nucleon was subtracted so that the missing mass ΔM should equal zero within experimental resolution and Fermi motion broadening. Examples, again integrated over the polar angle, are shown in Fig. 11. Residual background not removed by the coplanarity cut appears at large missing masses (mainly above 200 MeV) and is well separated from the events from single π^0 production.

The spectra are well reproduced by the results of the MC simulations, where the relative contributions of signal and background events were fitted to the data. Also, for these spectra, $\pm 1.5\sigma$ cuts were determined by the fits of a Gaussian distribution. These cuts are indicated in the figure by dotted vertical lines. The cuts at the low energy side are not necessary for the suppression of background. The tails at this side are due to large Fermi momenta. However, it is more convenient to use symmetric cuts because an asymmetric selection of Fermi momenta complicates further analysis.

The yields were finally extracted from the invariant mass spectra for which examples are shown in Fig. 12. The invariant mass $m_{\gamma\gamma}$ was evaluated from

$$m_{\gamma\gamma} = \sqrt{\left(\mathbf{P}_{\gamma_1} + \mathbf{P}_{\gamma_2}\right)^2} = \sqrt{2E_{\gamma_1}E_{\gamma_2}\left[1 - \cos\left(\phi_{\gamma_1,\gamma_2}\right)\right]}\,, \tag{7}$$

where $\mathbf{P}_{\gamma_1}$, $\mathbf{P}_{\gamma_2}$ are the four-momenta of the two π^0 decay photons, E_{γ_1}, E_{γ_2} are their energies, and ϕ_{γ_1,γ_2} is their opening angle. These spectra were evaluated as a function of the incident photon energy and cm-polar angle and agreed well with MC simulations. Cuts at $\pm 3\sigma$ were defined and are indicated in the figure.

Residual background was quite small and corresponds to the components visible in the cut region of the missing mass spectra. This background was subtracted before integration of the signals. Altogether, agreement between experimental data and MC simulations was excellent for all investigated kinematic quantities, indicating that systematic effects from the analysis are small (see Sec. III F for a quantitative discussion).

E. Reconstruction of final-state invariant mass W

The total cm energy W for the photoproduction of mesons off a nucleon target is given by

$$W = \sqrt{s} = \sqrt{(\mathbf{P}_\gamma + \mathbf{P}_N)^2} = \sqrt{\left(\sum_{i=1}^{n} \mathbf{P}_i\right)^2}\,, \tag{8}$$

where $\mathbf{P}_\gamma$ and $\mathbf{P}_N$ are the four-momenta of the incident photon and the target nucleon, and the $\mathbf{P}_i$, $i = 1,\ldots,n$ are the four-momenta of the final-state particles (emitted mesons and recoil nucleon all in the laboratory frame). For the most simple case of a free target nucleon at rest, this reduces to

$$W = \sqrt{2m_N E_\gamma + m_N^2}\,, \tag{9}$$

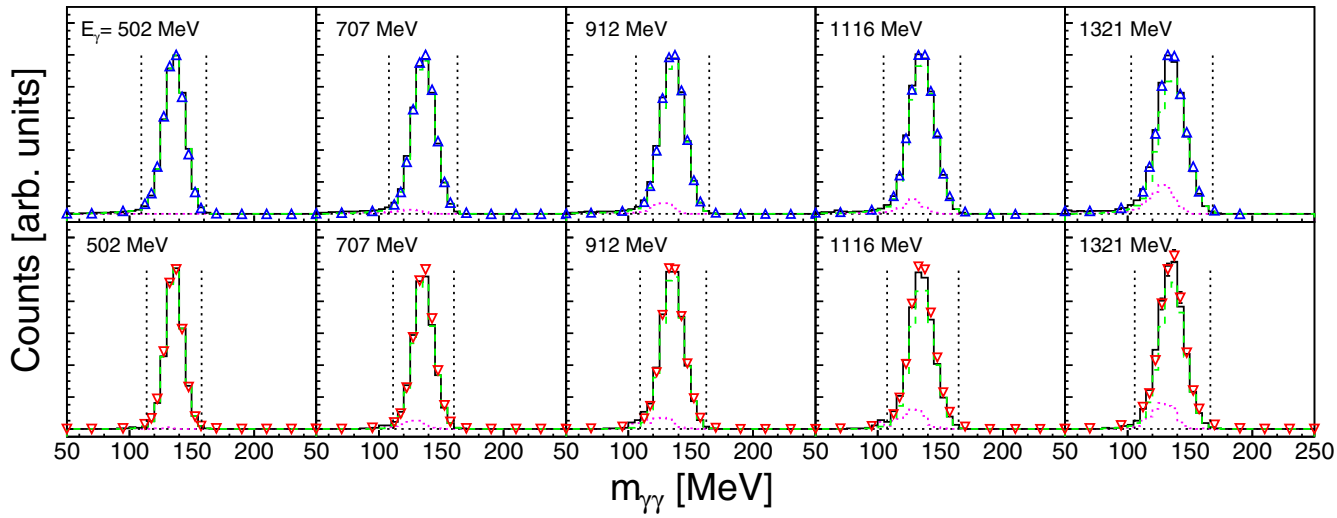

FIG. 12. Invariant mass distributions for several incident photon energies for exclusive single π^0 photoproduction off the quasifree proton (top, open upward blue triangles) and the quasifree neutron (bottom, open downward red triangles) integrated over the full angular range. Dashed green line, MC signal; dotted magenta line, sum of MC background contributions; solid black line, sum of MC signal and MC background; and dotted vertical lines, $\pm 3\sigma$ cut positions. PSA, χ^2 analysis for recoil neutrons, coplanarity, and missing mass cuts (as indicated in Figs. 10 and 11) were applied to the spectra.

with the photon beam energy E_γ and the mass m_N of the target. Nucleons bound in a nucleus are off-shell so that $\mathbf{P}_N^2 \neq m_N^2$ and each fixed value of incident photon energy corresponds to a distribution of W values, leading to the Fermi smearing of cross sections as a function of E_γ. However, this effect can be removed when W is not extracted from the incident photon energy, but from the right-hand side of Eq. (8), using the four-momenta of the final-state particles. The drawback of this method is that the resolution of the four-momenta of the final-state particles, measured with the production detector, is not as good as the resolution of the incident photon energy measured with the magnetic tagging spectrometer.

For this reconstruction, the measured four-momenta of the two decay photons were used. There is no direct, reliable measurement of the kinetic energy of neutrons detected in the CB. In TAPS, in principle, time of flight could be used, but the resolution would not be adequate. However, for the reconstruction of the final state W, it is sufficient to measure the polar and azimuthal angles of the recoil nucleon. The initial state, defined by the incident photon of known energy and the deuteron at rest, is completely determined. In the final state, the four-momenta of the decay photons and the direction of momentum of the participant nucleon are measured.

This means that the absolute magnitude of the momentum of the final-state recoil nucleon and the final-state three-momentum of the spectator nucleon are missing. These four kinematic quantities can, however, be recovered from the four boundary conditions due to energy and momentum conservation. For most recoil protons, the energy was directly measured by the calorimeters. However, in order to avoid additional systematic uncertainties in the comparison of neutron and proton cross sections, events with recoil protons were treated in the same way. This means that the energy information from the calorimeters was ignored in the reconstruction of all recoil nucleons.

This reconstruction also involves the determination of the polar angle of the emitted pion in the "true" cm system of the reaction (i.e., taking into account the momentum of the incident nucleon from Fermi motion). The reconstruction was done under the assumption of quasifree production, which means that the momenta of the incident-participant nucleon $\vec{q}_{p_i}$ and the final-state spectator nucleon $\vec{q}_{s_f}$ from the deuteron are related by $\vec{q}_{s_f} = -\vec{q}_{p_i}$.

As mentioned above, the measurement of W in the final state is influenced by the experimental resolution of the calorimeter for the photon momenta and the recoil nucleon angular resolution. This is shown in Fig. 13. The simulated

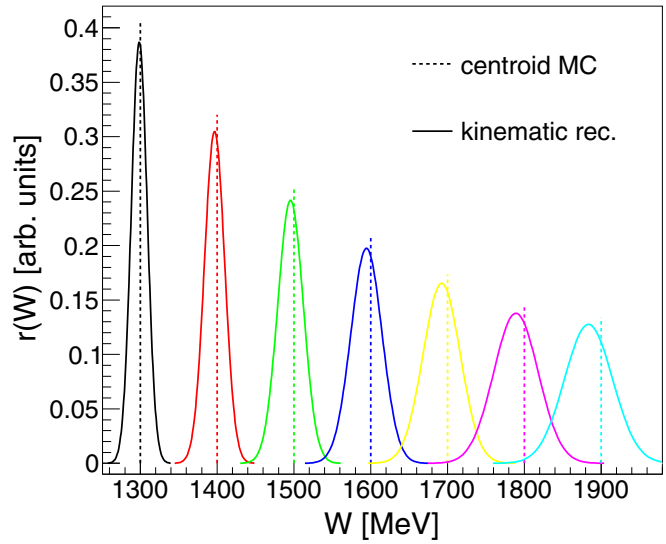

FIG. 13. Resolution for the final-state invariant mass W. The results of full MC simulations of the instrumental response are shown for given values of W (vertical lines).

response of the detector system is shown for selected values of W. The relative resolution varies in the range 2–4% FWHM for W between 1.3 and 1.9 GeV. Also, for the higher invariant masses, the maximum of the distributions is slightly shifted (maximum shift: 0.9%) with respect to the input centroid.

F. Absolute normalization and extraction of cross sections

The experimental yields for single pion production have been determined by integration of the invariant mass spectra (see Fig. 12 for examples) within the $\pm 3\sigma$ cut ranges. Background from random coincidences was already removed from all spectra in Sec. III D using the coincidence condition between tagging spectrometer and production detector, as discussed in detail in Ref. [57].

In addition, there was also background from the entrance and exit windows ($2 \times 125\,\mu$m Kapton) of the target cells which contained "heavy" nuclei, in particular, carbon. This background was determined with empty target measurements which were analyzed identically to the measurements with filled target cells. The corresponding yields, after normalization to the beam flux, were subtracted. Depending on the length of the target cells (4.72 or 3.02 cm) and on the final state of the reaction (with or without coincidence with recoil protons, neutrons), these background contributions ranged between 2% and 5%.

A trivial ingredient for the absolute normalization of the cross sections was the $\pi^0 \to \gamma\gamma$ decay branching ratio taken from the *Review of Particle Physics* (RPP) [73] as $(98.823 \pm 0.034)\%$.

Furthermore, a density of 0.169 g/cm^3 of the liquid deuterium was used, determined with measurements of the target pressure. This corresponds to a surface density of (0.231 ± 0.005) nuclei/b (4.72-cm target) and (0.147 ± 0.003) nuclei/b (3.02-cm target), which takes into account the shapes of the convex entrance and exit windows.

The incident photon flux was determined by a two-step measurement. The focal plane detectors of the tagging spectrometer were equipped with live-time gated scalers which recorded the flux of the scattered electrons as a function of their final-state energy. The tagging efficiency ϵ_t, which is the fraction of bremsstrahlung photons which pass the collimator and impinge on the production target, was regularly measured at reduced beam intensity, with the reduction made at the electron source and no change made to the accelerator parameters. For these measurements, a lead-glass detector was moved into the primary photon beam downstream from the production target. Typical tagging efficiencies were in the range 60–70%. Additionally, an ionization chamber placed downstream of the production target and just upstream of the dump of the photon beam monitored the flux in arbitrary units during the production measurements. The product $N_\gamma = N_{e^-} \times \epsilon_t$ of the electron rates in the tagger and the tagging efficiency was taken as the incident photon flux on the target.

An example of the flux distribution (measured with the 3-cm target) is shown in Fig. 14. The original spectrum was measured as a function of the energy of the bremsstrahlung photons. However, for the more important analysis, in terms of the reconstructed W of the final state, this was not the relevant quantity. The photon flux spectrum was folded with the effects of Fermi motion. The result is shown on the right-hand side of Fig. 14 as a function of effective W. Most of the structures from inefficient tagger channels are smeared out in this spectrum. Close to the upper edge of the distribution, the systematic uncertainties increase because the folding procedure assumes information about the photon flux at higher (untagged) photon energies.

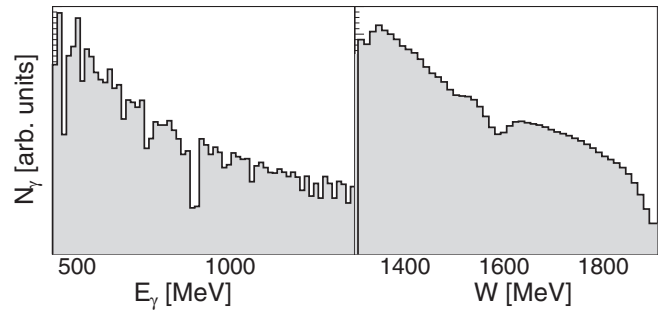

FIG. 14. Measured photon flux for the measurement with the 3 cm target. The left-hand side shows the flux measured as a function of photon energy. The structures in the spectrum are due to tagger channels with reduced efficiency. The right-hand side shows the flux as a function of reconstructed W after folding with the Fermi momentum distribution.

The most critical ingredient for the normalization of the yields is the instrumental detection efficiency. The basis for this is the MC simulation discussed in Sec. III C using the GEANT4 code [69]. However, further corrections, discussed below, had to be applied. Examples for the detection efficiency (taking into account corrections) as a function of the cm polar angle and for selected bins of incident photon energy are shown for single π^0 production in coincidence with recoil protons and neutrons in Fig. 15. Total detection efficiencies as a function of incident photon energy for these two exclusive reactions and for inclusive π^0 production without conditions for recoil nucleons are shown in Fig. 16. The detection efficiency for recoil neutrons was roughly in the 30% range, while recoil protons were detected with efficiency above 90%. The structure in the angular dependence of the detection efficiency for recoil protons is due to the transition region between CB and TAPS. This effect was less important for recoil neutrons, which are not affected so much by inactive materials. The detection efficiency at extreme pion-forward angles was very low, so that no results for pion-polar angles larger than $\cos(\theta_\pi^\star) > 0.9$ were obtained. This was caused by the experimental trigger conditions discussed below.

The agreement between the experimental results and the output from the MC simulations, as far as the shapes of the distributions of kinematic observables such as coplanarity, missing mass, and invariant mass discussed in Sec. III D are concerned, is excellent. However, there are two issues which required more detailed investigation.

The first arises from the hardware thresholds used in the experiment trigger and for the readout of the detector elements. The NaI modules of the CB detector were equipped with two leading edge discriminators (LED) per crystal and the modules

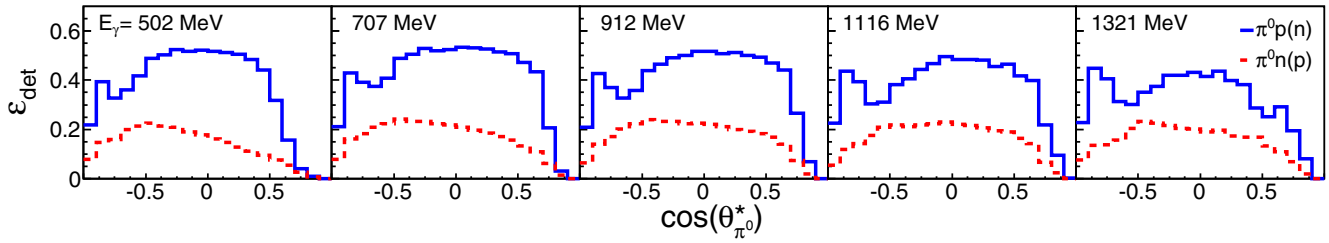

FIG. 15. Total detection efficiency based on MC simulations and including all corrections for the exclusive reactions $\gamma d \rightarrow p(n)\pi^0$ (solid, blue histograms) and $\gamma d \rightarrow n(p)\pi^0$ (dashed, red histograms) as a function of cm angle for the same bins of incident photon energy as in Figs. 10–12.

of the TAPS detector with an LED and a constant fraction discriminator (CFD) per crystal. The first discriminator system was used for trigger purposes and the second (in the case of TAPS, the CFDs) for the readout pattern of the detector.

For the trigger, as discussed in Sec. II, CB and TAPS were subdivided into logical sectors. If the signal from at least one crystal in a sector exceeded a threshold (≈30 MeV in CB, ≈35 MeV in TAPS) that sector contributed to the event multiplicity, which was two for the measurements discussed here. For events which satisfied the trigger condition, the second discriminator system with much lower thresholds (2 MeV for CB and 3–4 MeV for TAPS) generated the pattern of activated crystals from which energy and timing information was processed and stored. The discriminator thresholds were calibrated with the measured data and software thresholds above the maximum hardware thresholds were applied to experimental data and MC simulations in order to have well-defined conditions.

More involved was the implementation of the CB sum-threshold trigger in the simulations. This trigger was efficient for the selection of hadronic events and significantly reduced the count rate from electromagnetic background. It was set such that only events with a total energy deposition of roughly

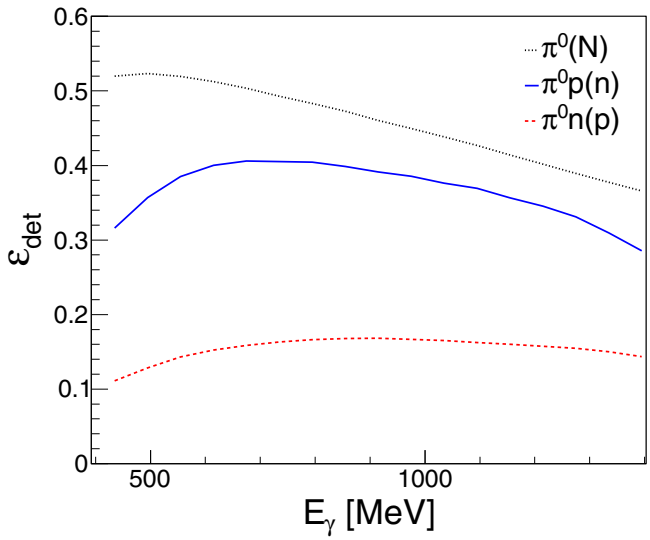

FIG. 16. Integrated detection efficiency as a function of incident photon energy E_γ for the inclusive reaction (dotted, black) and the exclusive reactions with detection of recoil protons (solid, blue) and recoil neutrons (dashed, red).

300 MeV in the CB were accepted. However, there were several systematic difficulties with it. A trivial one was that the energy deposition of recoil neutrons in the calorimeter is basically random. Depending on whether and where neutrons induce hadronic reactions, they can deposit very different amounts of energy and there is no correspondence between their kinetic energy and the energy they deposit in the calorimeter. To address this problem, events from the experimental data and also from the MC simulations were only accepted when the photon hits in the CB alone exceeded the sum threshold. Events where the recoil nucleon had to contribute to the sum trigger condition were discarded. This was also done for recoil protons in order to avoid systematic uncertainty in the comparison of proton and neutron data.

The sum-threshold trigger acted on the electronically generated analog sum of the uncalibrated output-voltage signals from the CB detector modules. The HV for the individual modules was set in a way that the deposited energy to output-voltage relation was similar for all crystals, but this was only an approximation. Therefore, the implementation of this trigger condition into the MC simulations required a detailed analysis. In the first step, the data were analyzed with a high software threshold for the analog sum (400 MeV instead of the nominal 300 MeV of the experiment) to make sure that all simulated events that pass this threshold would have also passed the hardware threshold. This gave a reasonable approximation of the energy and angular dependence of the cross section as input for further simulations of the effect of the hardware trigger. For the correct software implementation of the sum trigger, the experimental data and the results of the MC simulations had to be "decalibrated" because the hardware threshold acted on the sum of uncalibrated output voltages. Otherwise, the contribution of individual modules to the sum energy would have been over- or underestimated, depending on their calibration constants.

Figure 17 shows the experimental and simulated distributions of the CB sum energy for inclusive and exclusive reactions (upper row) and their ratio (lower row), where no energy sum threshold was applied in the simulations. The preset hardware energy threshold of 300 MeV is indicated in the lower row by the vertical lines.

The ratio was fitted by a cumulative distribution function of the type (red curves in Fig. 17),

$$f(E^{\mathrm{CB}}) = \frac{A}{1+\exp\left(\frac{\bar{E}-E^{\mathrm{CB}}}{B}\right)}, \tag{10}$$

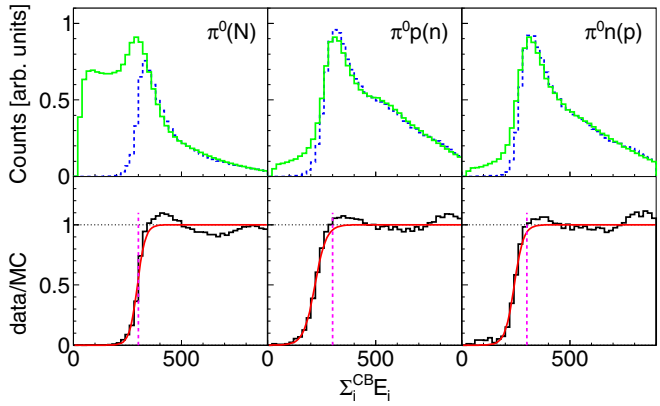

FIG. 17. Determination of the CB energy sum threshold. Upper row: raw count rates. Dashed (blue), experimental data; solid (green), MC simulation. Lower row: ratio of experimental data and simulation (black histogram). Smooth (red) curves: fit to data (see text). Vertical lines: preset hardware threshold. Both rows for inclusive data and data in coincidence with recoil protons and neutrons.

where A, B, and $\bar{E}$ are free parameters, the latter corresponding approximately to the applied hardware threshold. For the final simulation of detection efficiencies, MC events in the region where $f(E^{\mathrm{CB}})$ was zero were discarded, events where $f(E^{\mathrm{CB}}) = 1$ were accepted, and events in the transition region were weighted with $f(E^{\mathrm{CB}})$.

The second complication was due to the detection of the recoil nucleons. Protons and neutrons with relatively low kinematic energies were critical. Special packages for low energy nucleons were used in the MC simulations but, particularly in the transition region between CB and TAPS, this was not good enough. The material budget in the transition region between the CB and TAPS (inactive materials from support structures and cables) was not represented with sufficient accuracy in the MC simulations.

The resulting effects were negligible for photons, small for recoil neutrons, but significant for recoil protons. However, one should note that the simulation of neutron detection efficiencies is in general more involved than for protons. Therefore, detection efficiencies for recoil nucleons were cross checked with experimental data from measurements with a liquid hydrogen target. The reactions $\gamma p \to p\eta$ and $\gamma p \to p\pi^0\pi^0$ were analyzed for the detection efficiency of recoil protons and the reaction $\gamma p \to n\pi^0\pi^+$ for the detection efficiency of recoil neutrons. Single π^0 production off the proton could not be used because the hydrogen data were measured with a multiplicity-three trigger (for η production the $\eta \to 6\gamma$ decay was used). In both cases, the detection efficiency was model-independently extracted from the yields of the respective meson production reactions with and without detection of the recoil nucleons. A matrix of detection efficiency as a function of laboratory nucleon kinematic energies and polar angles was built. The same matrix was constructed for the MC simulations of the reactions from the free proton target. The ratio of these two distributions was then used to correct the simulated recoil nucleon detection efficiencies for the deuterium target. Typical corrections were below the $\pm 10\%$ level.

The results from the two beam times using the 4.72-cm target (140 h of beam time) and the 3.02-cm target (190 h), which had comparable statistical quality, were in excellent agreement and were averaged.

G. Systematic uncertainties

Global systematic uncertainties arose from the absolute normalization due to the target surface density and the incident photon flux. Also in this category was the uncertainty due to the subtraction of the contribution from the target-cell windows. These uncertainties were neither energy nor angle dependent (the empty target distribution might have been so, but was so small that this could not be investigated). They were estimated at 3% for the photon flux, 4% for target density (mainly due to uncontrolled deformations of the target cell in the cooled state), and 2.5% for the empty target subtraction (which is 50% of the total empty target yields and probably overestimated). The total overall uncertainty was estimated at 7%. This overall uncertainty is not included in the systematic uncertainty bands shown in the figures of the results in Sec. IV.

More important were the energy- and angle-dependent uncertainties from trigger conditions, analysis cuts, and MC simulations. They were estimated by varying the cut conditions in the analysis and by artificially replacing the hardware thresholds by higher software thresholds (e.g., the CB energy-sum threshold from 300 to 400 MeV). The empirical corrections to the recoil nucleon detection efficiencies were also taken into account.

Typical systematic uncertainties from these sources were around 5% for incident photon energies above 700 MeV and rose to about 15% for photon energies around 500 MeV. The largest systematic uncertainties arose at extreme forward and backward pion angles, in particular for low incident photon energies. This is mainly due to the CB sum-energy trigger. Decay photons from pions close to polar angles of 0° or 180° were not likely to hit the CB. Therefore, few events from very asymmetric decays of the pion triggered the sum threshold, which made this class of events prone to systematic effects from details of the hardware thresholds. Events at extreme pion-forward angles ($\cos(\theta_\pi^\star) > 0.9$) could not be analyzed because for such events, most decay photons were outside the angular range of the CB so that the sum threshold did not trigger.

H. Correction of final-state interaction effects

The production of mesons from quasifree nucleons bound in a nucleus is also influenced by final-state interactions. For the special case of pion production from the deuteron, such interactions may arise in the final-state NN system and/or the πN_s system (N_s: spectator nucleon). πN_p rescattering (N_p: participant nucleon) also contributes for reactions on a free proton target. The magnitude and the energy and angular dependence of FSI can differ significantly between reactions. Previous experiments have shown that FSI for η photoproduction off deuterons in the energy range discussed here is negligible for cross sections and also for polarization observables [42,57,66,74–76]. Also for photoproduction of

η' mesons, no significant effects were observed [43]. In the production of pion and $\pi\eta$ pairs, FSI was significant but moderate (typically in the 10–20% range, up to 30% for $\pi^0\eta$ pairs) [55,56,58,59,67]. Important FSI effects were also observed for the production of charged pions in the $\gamma d \to pp\pi^-$ reaction [44,45].

The present results for photoproduction of π^0 mesons show large deviations (see Sec. IV) between the results for free and quasifree protons bound in the deuteron. Most deviations are in the absolute scale of the cross section, while, apart from extreme forward angles, the shape of the angular distributions is not much affected. This observation is supported by the measurement of the helicity components of the total cross section: $\sigma_{3/2}$ (parallel photon and nucleon spin) and $\sigma_{1/2}$ (antiparallel spins) [35]. The ratio of the $\sigma_{1/2}$ and $\sigma_{3/2}$ components is almost identical for free and quasifree protons, with only the absolute scale of both cross sections modified.

For reactions with pions emitted at extreme forward angles, most of the momentum of the incident photon is transferred to the pion and the relative momentum between "participant" and "spectator" nucleons is small, giving rise to large NN FSI. This happens also for η and η' production. However, in contrast to pion production, those reactions are dominated by the E_{0+} multipole from the excitation of S_{11} nucleon resonances. This reaction mechanism requires a spin flip of the participant nucleon so that the two nucleons have antiparallel spin in the final state, while for pion production the deuteron-like configuration with parallel spins is more important, giving rise to very different NN FSI.

A model analysis of FSI for π^0 production off the deuteron [77] predicts that it is only significantly different for participant protons and neutrons at extreme forward pion angles (for which we do not have data). However, the absolute predicted scale of the effects for the proton target was not in quantitative agreement with observations, so that these predictions could not be used to correct the neutron data for FSI. Further modeling is under way [78], but there are not yet final results.

Currently, the only reasonable correction of the quasifree neutron results for FSI assumes that it is similar for protons and neutrons bound in the deuteron. For protons, it can be determined experimentally by a comparison of the reactions on free and quasifree protons. The ratio of these proton cross sections can then be used to correct the quasifree neutron cross section:

$$\frac{d\sigma_n^f}{d\Omega}(z,W) = \frac{d\sigma_n^{qf}}{d\Omega}(z,W) \times \frac{\langle d\sigma_p^f \rangle}{d\sigma_p^{qf}}(z,W), \qquad (11)$$

with $z = \cos(\theta_\pi^\star)$, and the subscripts p and n denote proton and neutron cross sections and the superscripts f and qf indicate free and quasifree cross sections.

However, one cannot directly compare measured quasifree and free proton cross sections. The energy resolution for the quasifree proton data includes the effects from the kinematic reconstruction of W for the final state, while W is directly taken from the incident photon energy measured with the tagging spectrometer for the free proton data. Because of this effect, structures such as the resonance bumps in the photoproduction of pions appear "dampened" for the quasifree reaction and the ratio of free to quasifree data develops artificial structures. Therefore, the measured free proton cross section $d\sigma_p^f/d\Omega(z,W)$ was not used in Eq. (11). Instead, this cross section was folded with the experimental resolution of the W reconstruction of the quasifree measurement. The result of the folding is denoted by $\langle d\sigma_p^f \rangle/d\Omega(z,W)$. This avoids artificial structures but does not correct the finite resolution effects.

An advantageous side effect of this FSI correction for the neutron cross section is that systematic uncertainties from this experiment (hardware thresholds, overall normalization, MC simulations of photon showers, etc.) cancel in Eq. (11) in the $d\sigma_n^{qf}/d\sigma_p^{qf}$ ratio (except those arising from the proton and neutron detection efficiencies).

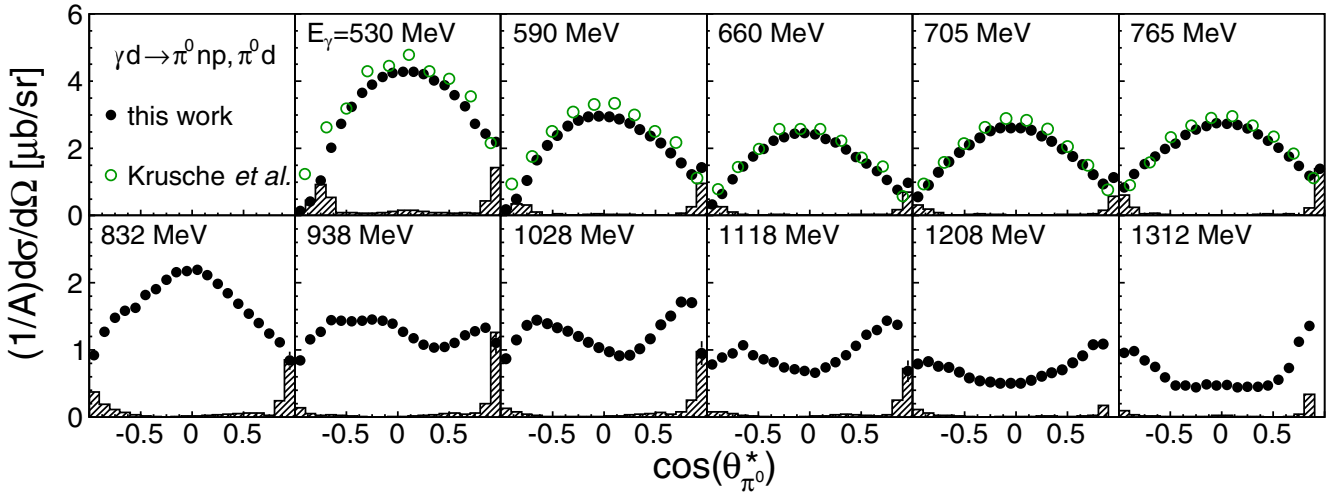

FIG. 18. Selected differential cross sections as function of the incident photon energy for quasifree inclusive single π^0 photoproduction compared to former results [39]. Full black circles, present results; open green circles, results from Ref. [39]. Cross sections normalized by $A = 2$, the number of nucleons (i.e., average nucleon cross section). Shaded bands: systematic uncertainty excluding 7% overall normalization uncertainty.

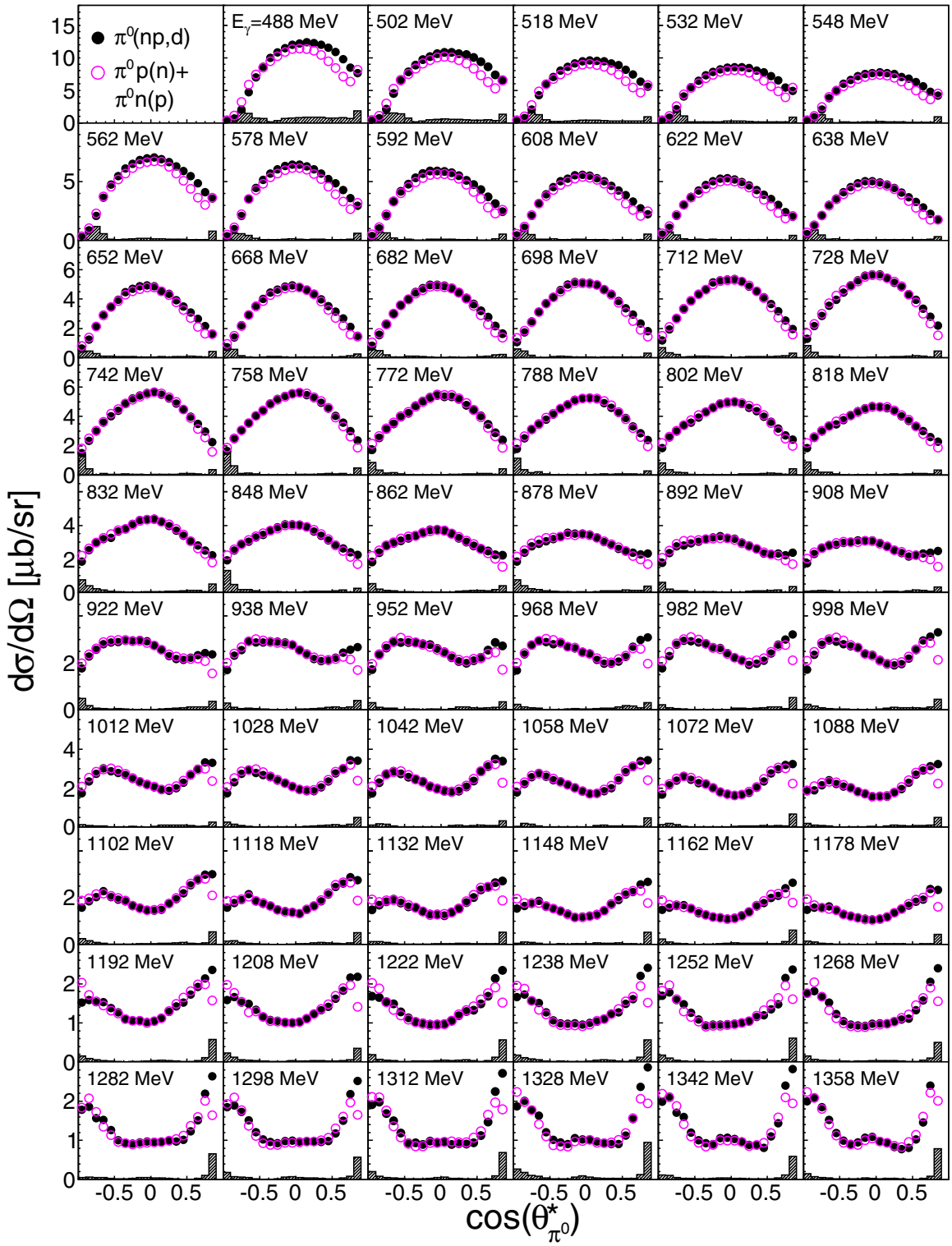

FIG. 19. Differential cross sections as a function of the cm polar angle for different bins of incident photon energy E_γ (central values of the bins are labeled in the figures). Black, filled dots correspond to the inclusive cross section $d\sigma_{\rm incl}/d\Omega$, including all single π^0 production reactions with a (np) or d final nucleon state. Magenta circles show the sum $d\sigma_p/d\Omega + d\sigma_n/d\Omega$ of the exclusive cross sections in coincidence with recoil protons and neutrons. The black histograms indicate the systematic uncertainty of the inclusive cross section (without the 7% overall normalization uncertainty).

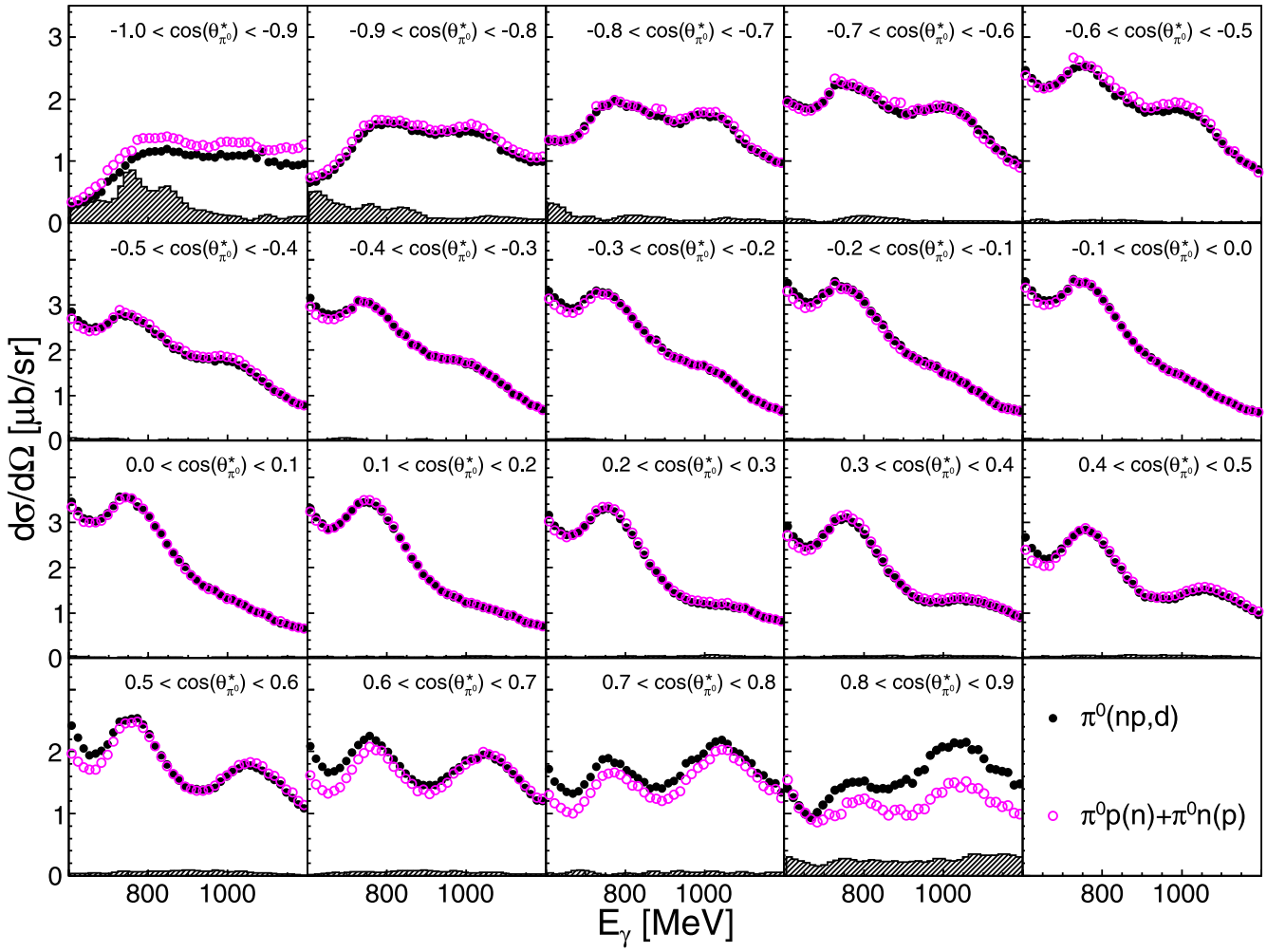

FIG. 20. Differential cross sections for the inclusive reaction $\gamma d \rightarrow \pi^0 X$ (black dots) and sum of exclusive cross sections (open magenta circles) as a function of the incident photon energy for different cm-polar angle bins. Notation as in Fig. 19.

For all results shown in the next section, it is mentioned in the figure captions when data have been corrected for FSI effects as described above. All other results are uncorrected quasifree data.

IV. RESULTS

First, we discuss the results for the inclusive cross section σ_{incl}. The only condition for such events was the identification of a π^0 meson and the exclusion of the production of further mesons by the missing mass analysis. An additional charged or neutral hit (due to recoil neutrons, recoil protons, or recoil deuterons) was accepted, but not required. This analysis was more prone to background than the exclusive analyses discussed below because coplanarity conditions could not be used. Also the kinematic reconstruction of the final state was not possible because a significant fraction of events, detected without a recoil nucleon, were kinematically under determined so that only the incident photon energy, measured by the tagging spectrometer, was available.

Several aspects of the results from the inclusive reaction, not discussed in the preceding letter [31], are interesting. First of all, these are the only results from the present experiment which can be compared to previous data. In Fig. 18, the present results for some typical energy bins are shown and compared to previous results from Ref. [39]. For the energy ranges where previous measurements are available, agreement of the shape of the angular distributions is excellent. The two results differ on an absolute scale by up to 10%. The overall normalization uncertainty for the two experiments is almost equal (7% for the present and 6% for the previous data [39]) so that no scale can be preferred. The agreement is not trivial because the instrumental detection efficiency (solid angle coverage) was very different for the two experiments (≈25% of the full solid angle for Ref. [39] and ≈93% of 4π for the present results). This corresponds to more than an order of magnitude in the detection efficiency for photon pairs. Also, the determination of the detection efficiency was done in different ways for the two experiments. For the results in Ref. [39], the detection efficiency was simulated in bins of laboratory polar angle and laboratory kinetic energy of the pions, while an event generator taking into account the roughly known angular distributions and effects of Fermi motion was used for the present results. Systematic uncertainties for these two approaches come from

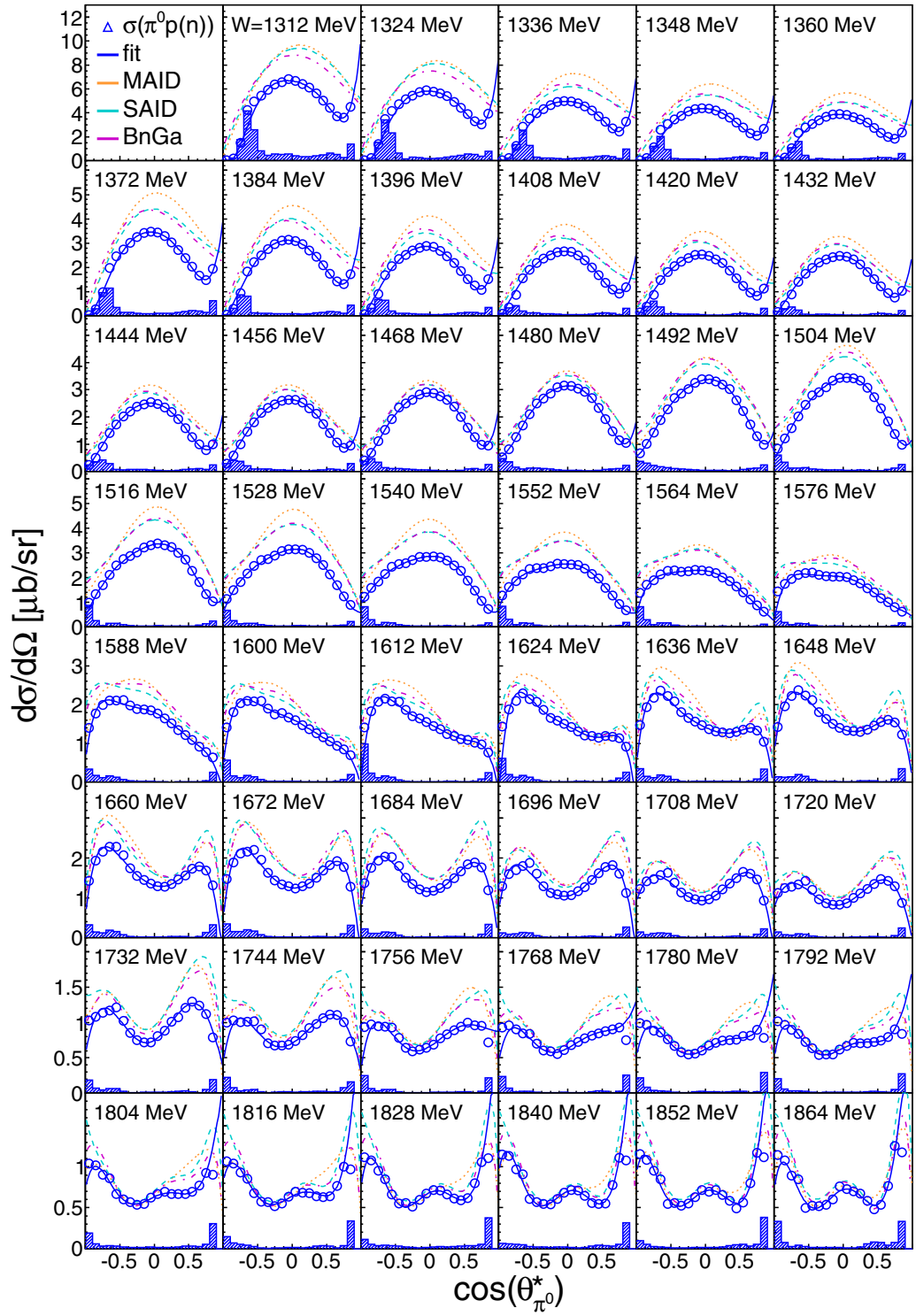

FIG. 21. Differential cross sections for exclusive single π^0 photoproduction off the quasifree proton. Open blue circles, experimental data; histograms, systematic uncertainty; and solid blue lines, Legendre fit to measured cross sections. Model results: dashed cyan line, SAID; dotted orange line, MAID; and dash-dotted magenta line, BnGa.

different sources. Results from earlier measurements with untagged photon beams and without discrimination against production of pion pairs are not shown; references can be found in Ref. [39].

Furthermore, a comparison of the results for the inclusive reaction and the exclusive reactions, in coincidence with recoil protons and recoil neutrons, provides stringent boundaries on systematic uncertainties for the detection of recoil protons

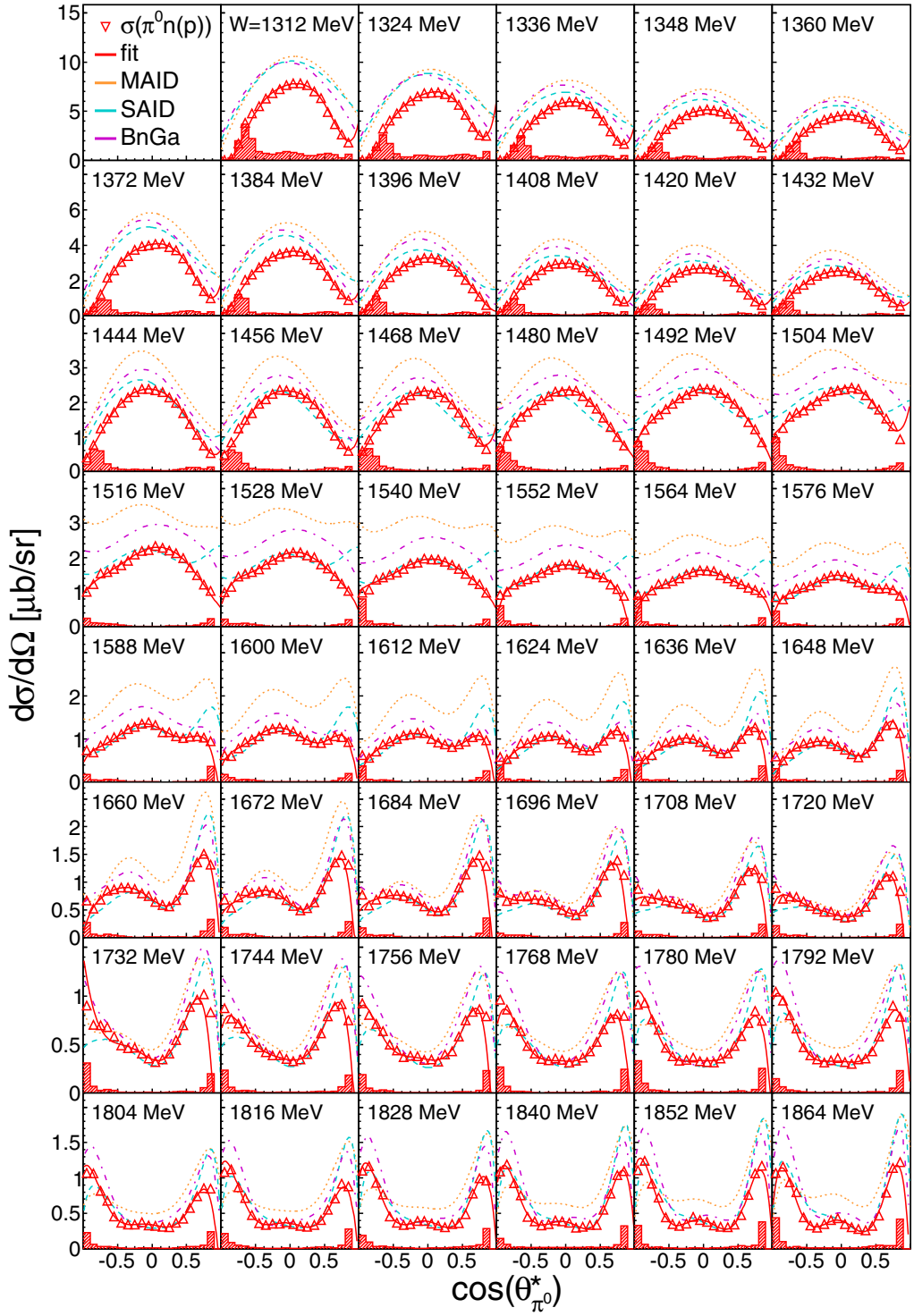

FIG. 22. Differential cross sections for exclusive single π^0 photoproduction off the quasifree neutron. Open red triangles, experimental data; histograms, systematic uncertainties; and solid red lines, Legendre fit to measured cross sections. Model results: dashed cyan line, SAID; dotted orange line, MAID; and dash-dotted magenta line, BnGa.

and recoil neutrons. The results for the inclusive reaction and the sum of the exclusive reactions are compared in Fig. 19 (angular distributions) and in Fig. 20 (excitation functions in bins of cm-polar angle). Apart from the extreme forward and backward angles (discussed below), the agreement between the two data sets is excellent. The inclusive cross section σ_{incl} depends only on the detection efficiency of the π^0-decay photons. The exclusive cross sections σ_p, σ_n also depend on the very different detection efficiencies of recoil protons ($>$90%) and recoil neutrons ($\approx$20–30%). Therefore, the good

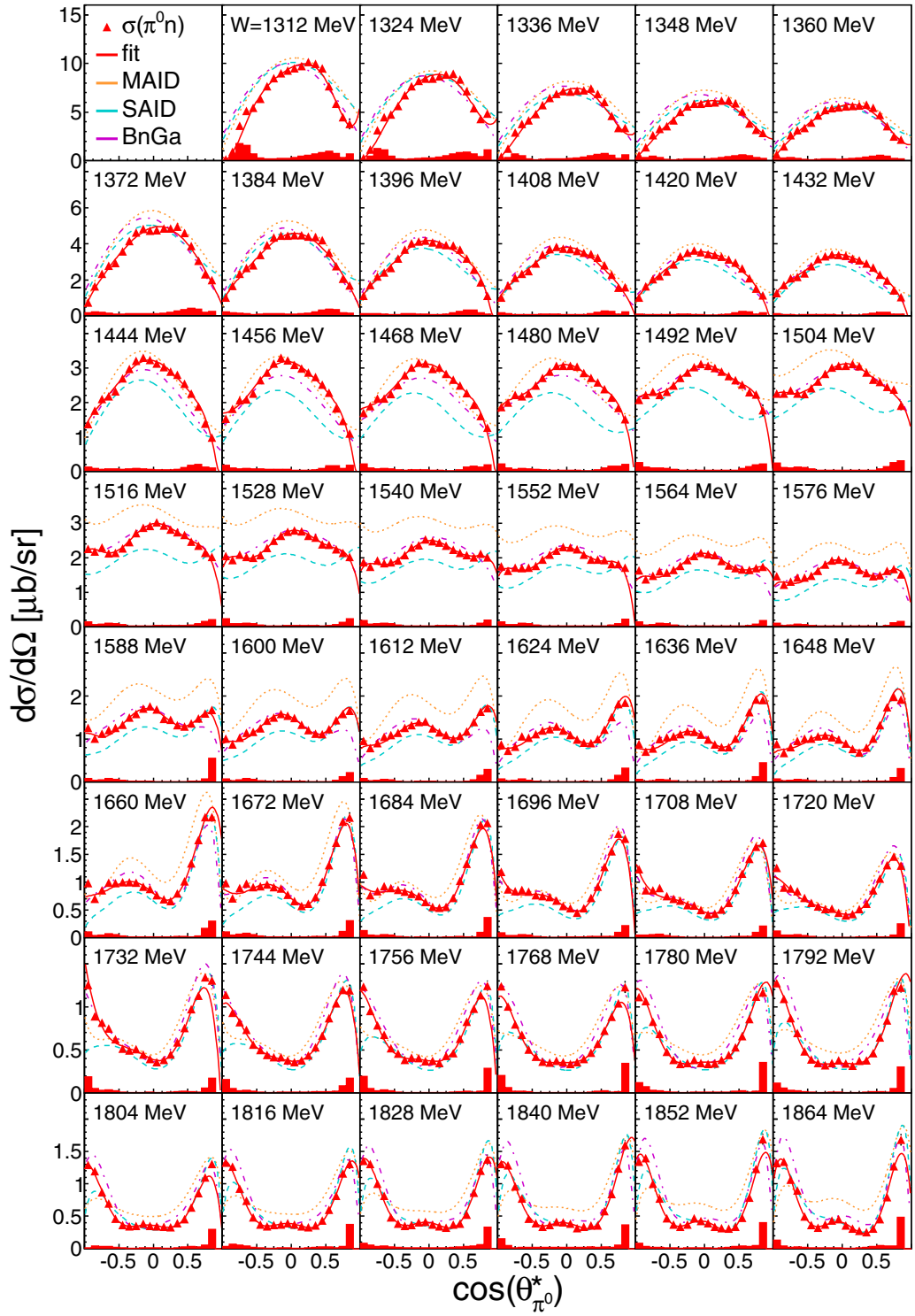

FIG. 23. Differential cross sections for exclusive single π^0 photoproduction off the free neutron (full red triangles). These are quasifree data corrected for FSI effects. Histograms, systematic uncertainties; and red solid lines, Legendre fit to measured data. Model results: dashed cyan lines, SAID; dotted orange lines, MAID; and dash-dotted magenta lines, BnGa.

agreement between the two analyses means that the recoil nucleon detection efficiencies are well under control. Similar results have previously been found for other reactions analyzed from the same data sample (η production [57], photoproduction of π^0 pairs [55] and of $\eta\pi$ pairs [58]). This is evidence that the detection of recoil nucleons is understood.

The deviations at extreme pion backward angles are within the quoted systematic uncertainties, which are mostly due

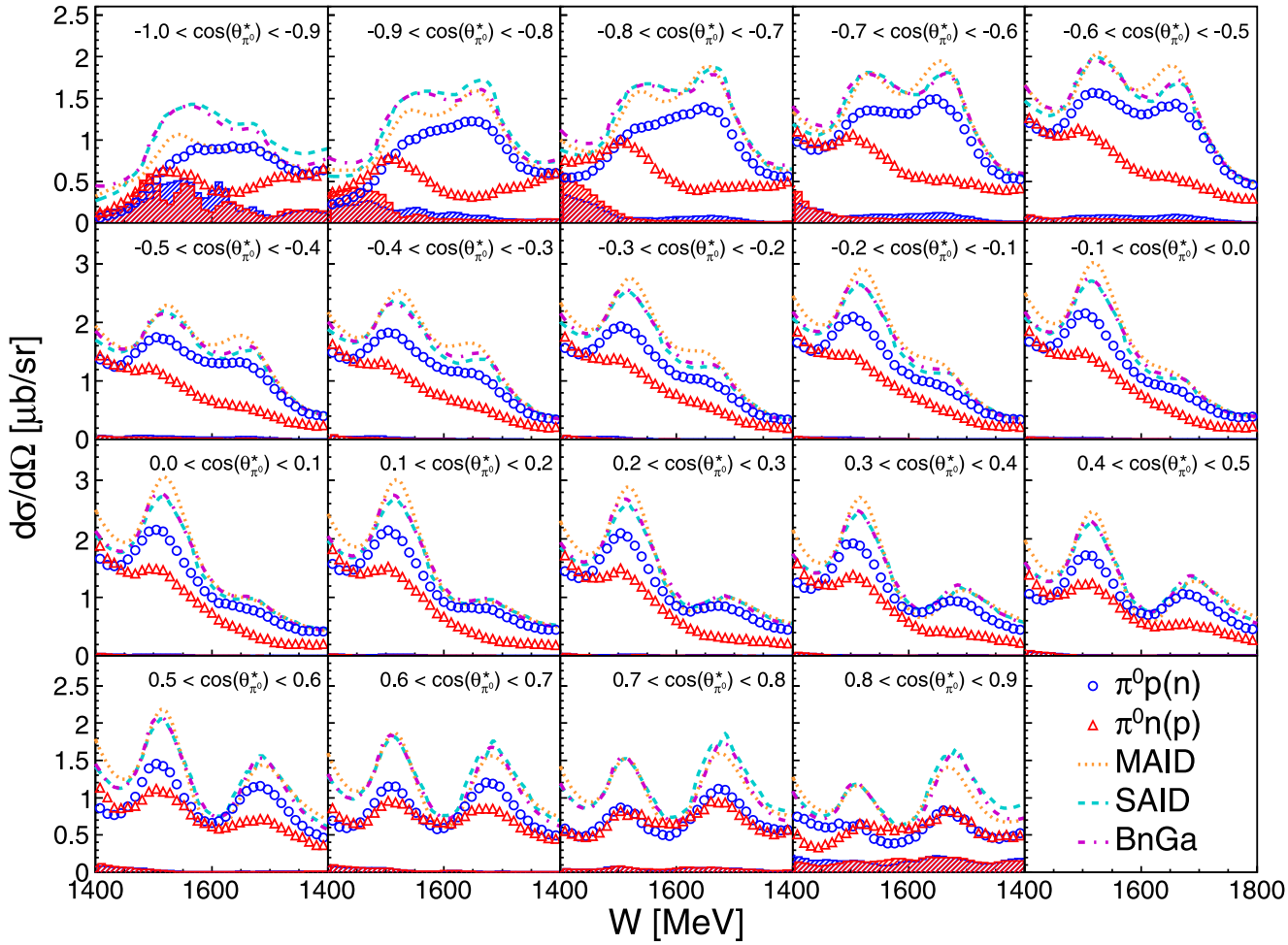

FIG. 24. Differential cross sections as a function of the final-state invariant mass for exclusive single π^0 photoproduction off the quasifree proton (blue, open circles) and the quasifree neutron (red, open triangles). Histograms: systematic uncertainties. Lines: model results for the free proton with notation as in Fig. 21.

to the sum-threshold trigger. However, this effect should be similar for the inclusive cross section and the sum of the exclusive cross sections because in both cases, only photons were accepted in the software trigger. Therefore, the quoted systematic uncertainty certainly overestimates the relative systematic uncertainty between the two results, but it should be considered when either result is compared to other data or model results. For the exclusive measurements, events with pions at extreme backward angles also require detection of recoil nucleons at extreme forward angles and at kinetic energies mostly in the punch-through regime. Such events have complicated detection efficiencies so that for this angular range, the inclusive analysis is more reliable than the result from the sum of the exclusive cross sections.

The situation for extreme pion forward angles is different. Systematic effects due to the sum trigger and the detection of the low-energy recoil nucleons are also important. However, there is also a physical reason for deviations because at extreme forward angles, coherent photoproduction of pions off the deuteron, the $\gamma d \to d\pi^0$ reaction, may contribute. Such events are included in the inclusive cross section but not in the exclusive cross sections where identification of recoil protons or neutrons is required. Therefore, as observed, the cross section for the inclusive reaction can be larger. This is also related to the FSI effects. Nucleon-nucleon FSI, which, when it leads to a binding of the two nucleons in the final state, will shift strength from the exclusive quasifree channels to the coherent reaction and thus deplete the exclusive reactions at forward angles. This makes the inclusive results interesting for testing models that investigate FSI effects.

The results for the exclusive, quasifree cross sections with detection of coincident recoil nucleons are summarized as angular distributions in Figs. 21 and 22, and as excitation functions for each angle bin in Fig. 24. The deviation of the quasifree proton data from the model results (see Figs. 21 and 24), which are only valid for free protons, is due to important FSI effects. The results from the SAID [1,2], MAID [3,4], and BnGa [6] models for the free $\gamma p \to p\pi^0$ reaction are almost identical because all models have been fitted to the same large database for the production of π^0 mesons off free protons.

The comparison of the present quasifree proton data to the consistent model results for the free proton cross section (see Fig. 21) demonstrates that the FSI effects vary in nontrivial

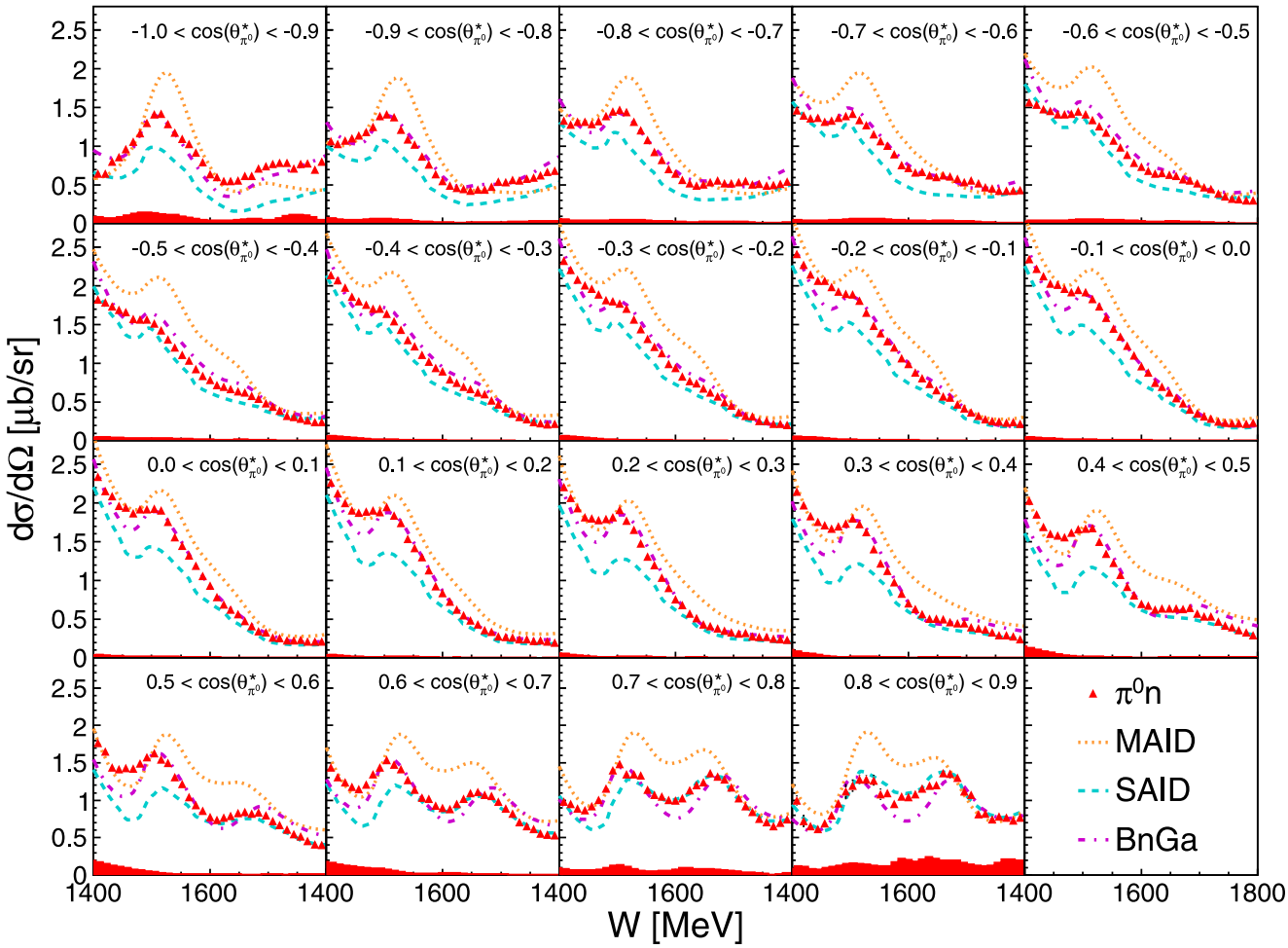

FIG. 25. Differential cross sections as a function of the final-state invariant mass for exclusive single π^0 photoproduction off the free neutron (i.e., quasifree neutron data with correction of FSI effects). Red triangles, experimental data; and histograms, systematic uncertainties. Notation for model results as indicated in Fig. 23.

ways. For example, they are much more important in the W range between 1500 and 1550 MeV (i.e., in the second resonance region) than in the tail of the Δ resonance between 1450 and 1480 MeV. The different behavior of the data for the $p\pi^0$ and $n\pi^0$ final state, which is best seen in Fig. 24, carries the physics information about the substantial isospin dependence of neutral pion production off protons and off neutrons.

Figures 23 and 25 show the results for the neutron target corrected for FSI under the assumption that FSI is equal for quasifree neutrons and protons [see Eq. (11)]. Note that systematic uncertainties (particularly visible when comparing Figs. 24 and 25) are very different from the quasifree data for neutrons because several systematic effects (related to trigger thresholds, empty target, photon detection, invariant mass analysis, etc.) cancel in Eq. (11). The 7% overall normalization uncertainty also does not apply. The residual uncertainty is dominated by the detection efficiency for recoil protons and neutrons (estimated from the comparison of inclusive data and the sum of exclusive cross sections), the systematic uncertainty of the world database for the cross section of the free $\gamma p \to p\pi^0$ reaction (which is negligible), and the folding of this cross section with the experimental resolution. Therefore, the systematic uncertainties for the extreme backward angles are much smaller for the FSI corrected results (see Fig. 25) than for the originally measured quasifree neutron data (see Fig. 24).

The data are compared in Figs. 21–25 to the most recent results from some reaction models (particularly those which provide results for the proton and neutron target). These are the BnGa coupled channel [6,79], MAID [3,4], and SAID [1,2] analyses. Note that the references refer only to the basic descriptions of the different analyses. The analyses evolve continuously and the most recent results are available on the respective websites [80].

In Figs. 21–25, only the most recent results from the three models are compared to the data. They are partly different from the results shown in the preceding Letter [31] because in the meantime, a larger database has been included in the fits of the BnGa and SAID analyses. This has not yet happened for the MAID model and Figs. 23 and 25 clearly show that this model is in poorer agreement with the experimental data. For the other models, some fine adjustments are still necessary.

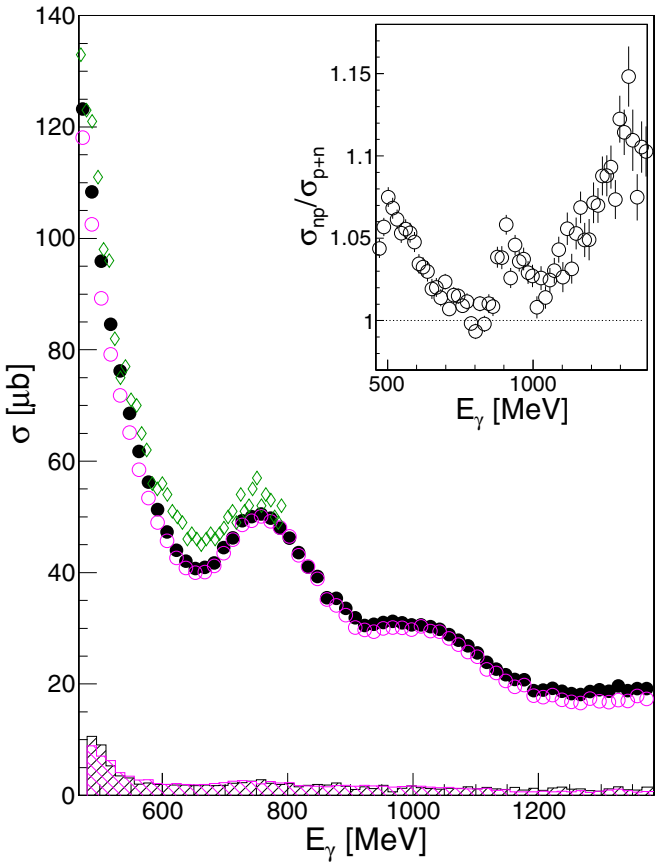

FIG. 26. Total cross section as a function of the incident photon energy for quasifree inclusive single π^0 photoproduction. Full (black) circles, quasifree inclusive data; open (magenta) circles, sum of quasifree proton and quasifree neutron total cross section; open (green) diamonds, MAMI 99 quasifree inclusive data [39]; and hatched histograms, systematic errors. Insert: ratio of the inclusive cross section and sum of the two exclusive cross sections.

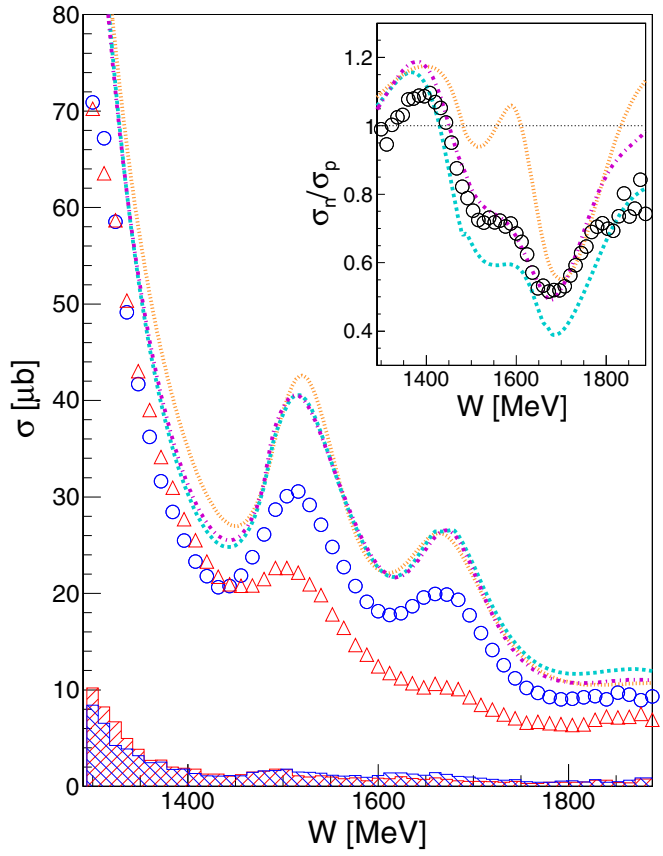

FIG. 27. Total cross section as a function of the final-state invariant mass for exclusive single π^0 photoproduction off the quasifree proton (open blue circles) and the quasifree neutron (open red triangles). Dashed cyan line, SAID; dotted orange line, MAID; and dash-dotted magenta line, BnGa. The insert shows the ratio of the quasifree neutron to the quasifree proton (open black circles).

Total cross sections $\sigma(W)$ have been derived from the angular distributions by fits of Legendre polynomials

$$\frac{d\sigma}{d\Omega} = \sum_{i=0}^{6} B_i P_i[\cos(\Theta^{\star}_{\pi^0})], \tag{12}$$

using $\sigma(W) = 4\pi B_0(W)$. The order of the expansion ($n = 6$) was chosen such that the coefficient of this order was still significantly different from zero within statistical uncertainties. This analysis extrapolates the unmeasured differential cross sections at extreme forward angles. This effect is small below energies of $W \approx 1.6$ GeV but contributes more to the systematic uncertainty at larger W.

The total cross section $\sigma_{\rm incl}$ for the inclusive reaction is shown as a function of E_γ in Fig. 26. The result from the inclusive analysis without any conditions on recoil nucleons and the sum of the exclusive cross sections σ_p and σ_n are compared. The agreement between the two data sets is excellent and demonstrates again that systematic effects from the detection efficiency for the recoil nucleons must be small. The insert in the figure shows the ratio of the results from these two analyses. Deviations are within the 10% range, but mostly smaller. The ratio is always above unity, which is reasonable because the sum of the exclusive cross sections excludes the contribution from the coherent $\gamma d \to d\pi^0$ reaction. At photon energies below 800 MeV, this effect alone can explain the deviations (see Ref. [39] for the relative contribution of the coherent reaction), at higher incident photon energies systematic uncertainties probably dominate.

For photon energies below 800 MeV, the present data can be compared to the previous results from Ref. [39]. They agree within their systematic uncertainties (typical deviations are of the order of 10%, the overall normalization of both data sets is ≈7%, and additional uncertainties from analysis cuts, etc., are ≈5%).

The total cross sections for the quasifree reactions $\gamma d \to p(n)\pi^0$ and $\gamma d \to n(p)\pi^0$ (spectator nucleons in parentheses) are shown in Fig. 27. The results are compared to the predictions of the BnGa, MAID, and SAID analyses for the free proton target. These predictions are similar, constrained by the same, large database of the free $\gamma p \to p\pi^0$ reaction. The figure demonstrates the substantial FSI effect on the quasifree reaction even when nucleons are only bound in the lightest nucleus, the deuteron. In the maxima of the second resonance

bump, this effect is on the order of 37% and in the third resonance bump it is still around 30%.

In addition, the figure shows that the second and, even more so, the third resonance bumps are much less pronounced for quasifree neutrons than for protons, while, due to the dominant reaction mechanism, these two cross sections are quite similar in the tail of the Δ resonance, as expected. This result sheds some new light on the suppression of the second and third resonance bumps in the total photoabsorption on the deuteron compared to the free proton target [30]. Obviously, both mechanisms mentioned in the introduction play a role: The quasifree reaction on protons is damped compared to the free proton due to FSI effects, in particular in the maxima of the resonance peaks. Furthermore, both resonance peaks are much less pronounced for the quasifree neutron than for the proton. This is due to the isospin structure of the excitation of the nucleon resonances involved. The insert in the figure shows the ratio of the total neutron and proton cross sections compared to model predictions. The SAID and BnGa analyses are in fair agreement with the measurements, but the MAID analysis overestimates the contribution of the $N(1525)3/2^-$ resonance for the neutron.

The results for the total cross section for $\gamma n \to n\pi^0$ [i.e., the quasifree $\gamma d \to \pi^0 n(p)$ data after removing effects from Fermi motion and with FSI corrections] are compared to model predictions in Fig. 28. The experimental data are slightly changed with respect to the results shown in Ref. [31] due to an improved treatment of the experimental resolution in the FSI correction.

The results from the SAID and BnGa analyses, prior to the present experimental results and prior to the data from Ref. [35] for the helicity dependence of the reaction, are also shown. They highlight the impact of the new quasifree neutron data. Closest to the experimental results is the most recent fit of the BnGa model (note the large change of the results from this model compared to the previous fit). Agreement is slightly worse with the SAID results which did not much change by the inclusion of the recent quasifree data. The MAID analysis clearly needs to be updated with inclusion of the recent quasifree data.

The experimental results for the σ_n/σ_p ratio given in Figs. 27 and 28 are quite similar. The values in Fig. 27 were directly obtained as a ratio of the measured total quasifree cross sections $\sigma_n^{qf}/\sigma_p^{qf}$. The results in Fig. 28 represent the ratio σ_n^f/σ_p^f. Since $d\sigma_n^f/d\Omega$ was calculated from $d\sigma_n^{qf}/d\Omega$ by application of the FSI correction factors $\langle d\sigma_p^f\rangle/d\sigma_p^{qf}$ (see Sec. III H), the correction cancels as long as it is independent on the polar angle $\theta_\pi^\star$ (which it almost is).

The behavior of the angular distributions is reflected in the coefficients of the Legendre polynomials [Eq. (12)] fitted to the experimental data. They are shown in Fig. 29 for the quasifree data and in Fig. 30 for the extracted free neutron data. All coefficients are normalized to the leading B_0, which is proportional to the total cross section. Model results from BnGa, MAID, and SAID for the free proton are compared to the data in Fig. 29, and those for the free neutron from the same analyses are shown in Fig. 30. All model results were obtained by fits of the angular distributions with Eq. (12) exactly as in

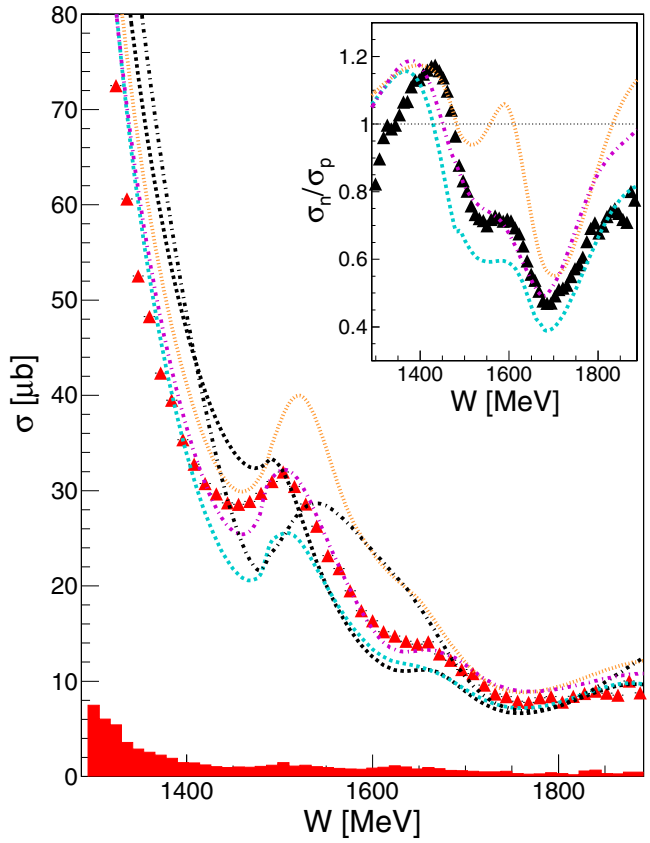

FIG. 28. Full red triangles: Total cross section as a function of the final-state invariant mass for the free neutron (quasifree neutron data corrected for FSI effects). Dashed cyan line, SAID; dotted orange line, MAID; and dash-dotted magenta line, BnGa. The black dashed and dash-dotted lines show the results of the SAID and BnGa analysis previous to the results from the present work and Ref. [35]. The insert shows the ratio of the free neutron to the SAID proton (full black triangles).

the treatment of the experimental data. Figure 29 highlights the differences between the $\gamma p \to p\pi^0$ and $\gamma n \to n\pi^0$ reactions for higher partial waves, which usually do not leave large signals in the total cross section. In particular, around invariant masses of 1.7 GeV—in the third resonance region—large signals are seen in the B_3 and B_5 coefficients for the neutron target.

When such proton-neutron differences are due to resonance excitations, only $N^\star$ states can be responsible since electromagnetic Δ excitations are not isospin dependent. It was already emphasized in the preceding Letter [31] that, for example, in the BnGa model, a refit to the previously existing database *and* the new neutron data mainly modified the resonant isospin $I = 1/2$ partial waves and nonresonant backgrounds. The $I = 3/2$ partial waves were much more stable because they are better constrained by the data for the free $\gamma p \to p\pi^0$ reaction.

In the energy region around $W = 1.7$ GeV, two $N^\star$ resonances with spin $J = 5/2$ contribute, the $N(1675)5/2^-$ (D_{15} partial wave) and the $N(1680)5/2^+$ (F_{15}). According to RPP

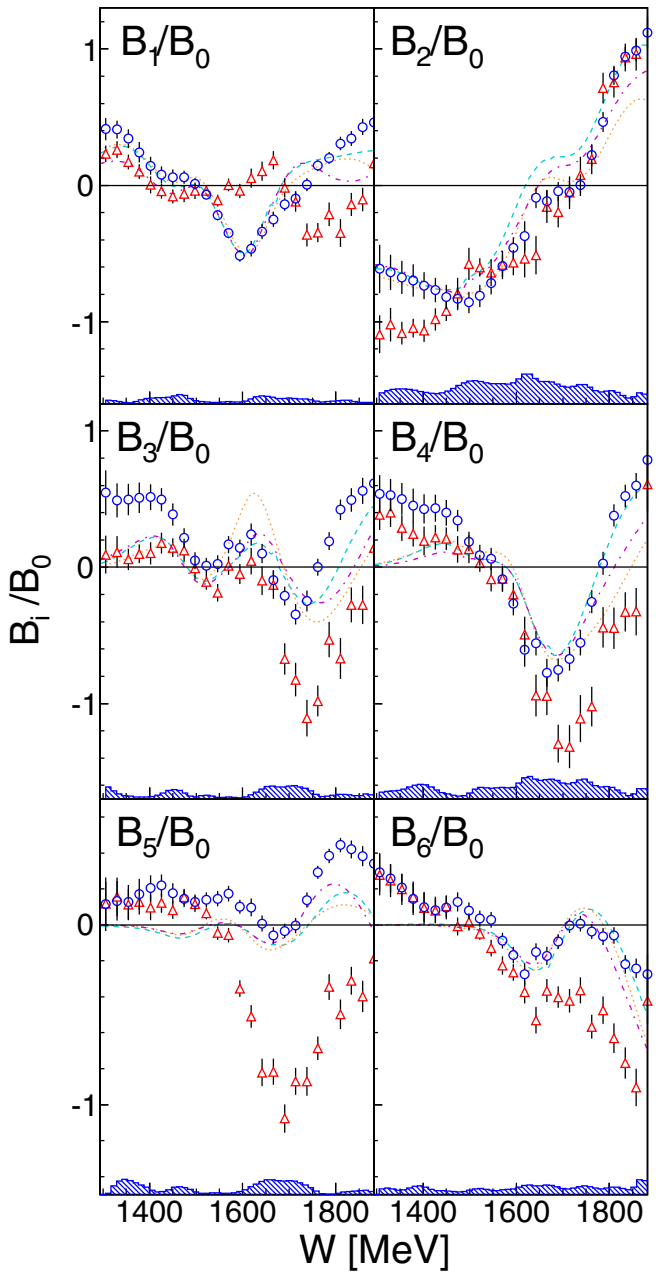

FIG. 29. Normalized Legendre coefficients as a function of the final-state invariant mass for exclusive single π^0 photoproduction off the quasifree proton (open blue circles) and the quasifree neutron (open red triangles). Hatched histograms: systematic uncertainties of the quasifree proton. Dashed cyan curve, SAID; dotted orange curve, MAID; and dash-dotted magenta curve, BnGa.

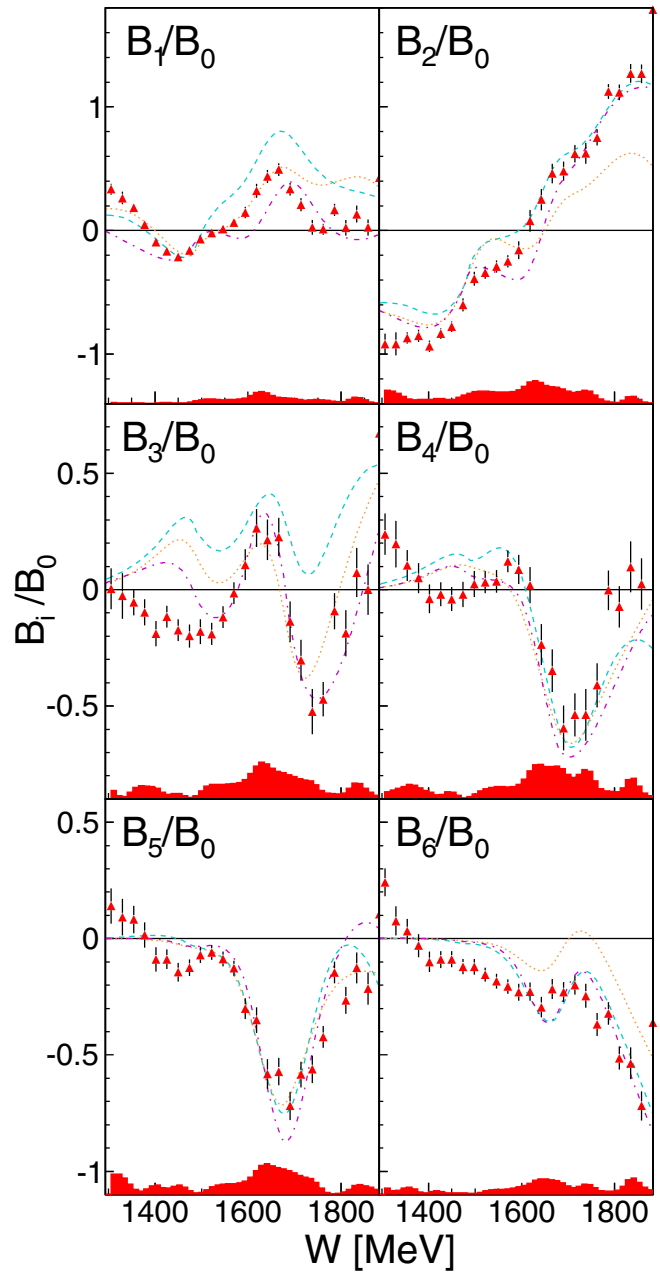

FIG. 30. Full red triangles: normalized Legendre coefficients as a function of the final-state invariant mass for exclusive single π^0 photoproduction off the free neutron (quasifree data corrected for FSI effects). Solid histograms, systematic uncertainties; dashed cyan curve, SAID; dotted orange curve, MAID; and dash-dotted magenta curve, BnGa.

[73], the F_{15} has a much larger electromagnetic coupling to the proton and is responsible for a large fraction of the third resonance bump for the proton. The D_{15} is one of the few states which couple more strongly to the neutron. Its influence on the angular distributions seems to be well reproduced by the BnGa and MAID model results, but significant deviations are observed for the B_3 coefficient in this energy range for SAID (see Fig. 30).

In Fig. 30, the Legendre coefficients of the free $\gamma n \to n\pi^0$ reaction (constructed from the FSI corrected quasifree neutron data) are compared to the reaction model results. A comparison of the quasifree (Fig. 29) and "free" (Fig. 30) neutron data does not show much difference (the largest for the B_3 coefficient). This is again due to the fact that FSI seems mainly to act on the absolute scale of the cross sections (which is removed by the renormalization to the B_0 coefficient), but not so much

on the shape of the angular distributions. The comparison to the model predictions does not allow a clear conclusion. Although on average, the MAID analysis agrees less well with the total cross section than the SAID results, some features, such as the behavior of the B_3 coefficient at high energies, are better reproduced by MAID than by SAID. Altogether, all reaction models will need readjustment to accommodate the new neutron measurements.

V. SUMMARY AND CONCLUSIONS

Photoproduction of π^0 mesons from the deuteron has been measured in a high statistics experiment with the Crystal Ball/TAPS detector at the electron accelerator MAMI in Mainz for incident photon energies between 0.45 and 1.4 GeV, corresponding approximately to cm energies in the photon-nucleon system of 1.3 to 1.875 GeV. Angular distributions were obtained in bins of $\cos(\theta^\star_{\pi^0}) = 0.1$ and only the extreme forward bin from 0.9 to 1.0 was not covered. Data have been analyzed for the inclusive reaction $\gamma d \to X\pi^0$, where X is either a neutron-proton pair or a deuteron. The reaction was identified by detection of the π^0 mesons and kinematic cuts excluding production of further mesons. Also analyzed were the exclusive reactions $\gamma d \to p\pi^0(n)$ and $\gamma d \to n\pi^0(p)$ in coincidence with recoil protons or recoil neutrons where the nucleons in parentheses are undetected spectators.

A comparison of the results from the inclusive reaction $\sigma_{\rm incl}$ to the sum of the exclusive reactions σ_p, σ_n sets stringent limits on systematic uncertainties of the detection of recoil nucleons because $\sigma_{\rm incl}$ is completely independent of such effects. The inclusive data are of interest for the investigation of FSI effects because all event classes with production of one π^0 and no further meson are included without discrimination against different baryonic final states.

The most interesting experimental information comes from the investigation of the $\gamma n \to n\pi^0$ reaction. The present results represent the first comprehensive data set for this reaction. The comparison to proton data demonstrates clearly the large isospin dependence of this reaction. The comparison to model results and PWA shows that analyses based only on data from the other three isospin channels (the final states $p\pi^0$, $n\pi^+$, $p\pi^-$) are not sufficiently constrained. This was expected because the model predictions disagreed significantly among themselves, but it was also demonstrated, by the refit of one model, that the present and the previous data from other isospin channels can be accommodated in the same fit when the critical partial waves (particularly those from excitations of $N^\star$ resonances and nonresonant backgrounds) are properly adjusted.

These results are not completely model independent. Originally, the quasifree $\gamma d \to n\pi^0(p)$ reaction was measured with a detected "participant" neutron and an undetected "spectator" proton. The effective invariant mass W of the intermediate state of the photon and the participant nucleon depends on nuclear Fermi motion. This effect was removed by using the invariant mass W derived from the detected pion and the final-state participant nucleon. The resolution obtained for W, reconstructed this way, depends on the detector resolution of the four momenta of the particles, rather than on the much better resolution of the momenta of the degraded electrons in the tagging spectrometer.

Effects from nuclear FSI have been corrected under the assumption that it is equal for participant protons and neutrons. The ratio of free ($\gamma p \to p\pi^0$) and quasifree [$\gamma d \to p\pi^0(n)$] proton production cross sections was used to correct the quasifree neutron data. The available results from modeling FSI effects [77] support the assumption that, for the angular range covered by the experimental data, they are similar for participant protons and neutrons. However, these results [77] are not in quantitative agreement with the experimental proton data so that further refinements of the FSI modeling are required before it can be used for reliable FSI corrections of quasifree neutron data.

It is obvious from the comparison of the most recent reaction model analyses from BnGa, MAID, and SAID [2,4,79] to the present neutron data that these analyses still need refinements, which will help to establish a more solid database for electromagnetic excitations of neutron $N^\star$ resonances.

ACKNOWLEDGMENTS

We wish to acknowledge the outstanding support of the accelerator group and operators of MAMI. This work was supported by Schweizerischer Nationalfonds (200020-156983, 132799, 121781, 117601), Deutsche Forschungsgemeinschaft (SFB 443, SFB 1044, SFB/TR16), the INFN-Italy, the European Community-Research Infrastructure Activity under the FP7 programme (Hadron Physics, Grant Agreement No. 227431), the UK Science and Technology Facilities Council (ST/J000175/1, ST/G008604/1, ST/G008582/1,ST/J00006X/1, and ST/L00478X/1), and the Natural Sciences and Engineering Research Council (NSERC, FRN: SAPPJ-2015-00023), Canada. This material is based upon work also supported by the U.S. Department of Energy, Office of Science, Office of Nuclear Physics Research Division, under Awards No. DE-FG02-99-ER41110, No. DE-FG02-88ER40415, and No. DE-FG02-01-ER41194 and by the National Science Foundation under Grants No. PHY-1039130 and No. IIA-1358175.

[1] R. A. Arndt, W. J. Briscoe, I. I. Strakovsky, and R. L. Workman, Phys. Rev. C **66**, 055213 (2002).

[2] R. L. Workman, M. W. Paris, W. J. Briscoe, and I. I. Strakovsky, Phys. Rev. C **86**, 015202 (2012).

[3] D. Drechsel, O. Hanstein, S. S. Kamalov, and L. Tiator, Nucl. Phys. A **645**, 145 (1999).

[4] D. Drechsel, S. S. Kamalov, and L. Tiator, Eur. Phys. J. A **34**, 69 (2007).

[5] S. S. Kamalov, S. N. Yang, D. Drechsel, O. Hanstein, and L. Tiator, Phys. Rev. C **64**, 032201(R) (2001).
[6] A. V. Anisovich *et al.*, Eur. Phys. J. A **44**, 203 (2010).
[7] T. Feuster and U. Mosel, Nucl. Phys. A **612**, 375 (1997).
[8] T. Feuster and U. Mosel, Phys. Rev. C **59**, 460 (1999).
[9] C. Fernandez-Ramirez, E. Moya de Guerra, and J. M. Udias, Ann. Phys. **321**, 1408 (2006).
[10] D. Rönchen *et al.*, Eur. Phys. J. A **49**, 44 (2013).
[11] M. Shrestha and D. M. Manley, Phys. Rev. C **86**, 055203 (2012).
[12] I. G. Anznauryan *et al.*, Phys. Rev. C **80**, 055203 (2009).
[13] O. Bartholomy *et al.*, Phys. Rev. Lett. **94**, 012003 (2005).
[14] O. Bartalini *et al.*, Eur. Phys. J. A **26**, 399 (2005).
[15] H. Van Pee *et al.*, Eur. Phys. J. A **31**, 61 (2007).
[16] M. Dugger *et al.*, Phys. Rev. C **76**, 025211 (2007).
[17] D. Elsner *et al.*, Eur. Phys. J. A **39**, 373 (2009).
[18] N. Sparks *et al.*, Phys. Rev. C **81**, 065210 (2010).
[19] V. Crede *et al.*, Phys. Rev. C **84**, 055203 (2011).
[20] A. Thiel *et al.*, Phys. Rev. Lett. **109**, 102001 (2012).
[21] M. Gottschall *et al.*, Phys. Rev. Lett. **112**, 012003 (2014).
[22] M. H. Sikora *et al.*, Phys. Rev. Lett. **112**, 022501 (2014).
[23] S. Schumann *et al.*, Phys. Lett. B **750**, 252 (2015).
[24] P. Adlarson *et al.*, Phys. Rev. C **92**, 024617 (2015).
[25] J. Hartmann *et al.*, Phys. Lett. B **748**, 212 (2015).
[26] J. R. M. Annand *et al.*, Phys. Rev. C **93**, 055209 (2016).
[27] S. Gardener *et al.*, Eur. Phys. J. A **52**, 333 (2016).
[28] A. Thiel *et al.*, Eur. Phys. J A **53**, 8 (2017).
[29] B. Krusche and S. Schadmand, Prog. Part. Nucl. Phys. **51**, 399 (2003).
[30] B. Krusche, Eur. Phys. J. Special Topics **198**, 199 (2011).
[31] M. Dieterle *et al.*, Phys. Rev. Lett. **112**, 142001 (2014).
[32] P. T. Mattione *et al.*, Phys. Rev. C **96**, 035204 (2017).
[33] D. Ho *et al.*, Phys. Rev. Lett. **118**, 242002 (2017).
[34] R. Di Salvo *et al.*, Eur. Phys. J. A **42**, 151 (2009).
[35] M. Dieterle *et al.*, Phys. Lett. B **770**, 523 (2017).
[36] J. Ahrens *et al.*, Eur. Phys. J. A **44**, 189 (2010).
[37] W. T. Chiang and F. Tabakin, Phys. Rev. C **55**, 2054 (1997).
[38] M. Fuchs *et al.*, Phys. Lett. B **386**, 20 (1996).
[39] B. Krusche *et al.*, Eur. Phys. J. A **6**, 309 (1999).
[40] K. Büchler *et al.*, Nucl. Phys. A **570**, 580 (1994).
[41] P. Benz *et al.*, Nucl. Phys. B **65**, 158 (1973).
[42] I. Jaegle *et al.*, Eur. Phys. J. A **47**, 89 (2011).
[43] I. Jaegle *et al.*, Eur. Phys. J. A **47**, 11 (2011).
[44] V. E. Tarasov, W. J. Briscoe, H. Gao, A. E. Kudryavtsev, and I. I. Strakovsky, Phys. Rev. C **84**, 035203 (2011).
[45] W. Chen, H. Gao, W. J. Briscoe, D. Dutta, A. E. Kudryavtsev, M. Mirazita, M. W. Paris, P. Rossi, S. Stepanyan, I. I. Strakovsky *et al.*, Phys. Rev. C **86**, 015206 (2012).
[46] W. J. Briscoe, A. E. Kudryavtsev, P. Pedroni, I. I. Strakovsky, V. E. Tarasov, and R. L. Workman, Phys. Rev. C **86**, 065207 (2012).
[47] E. M. Darwish, H. Arenhövel, and M. Schwamb, Eur. Phys. J. A **16**, 111 (2003).
[48] K. Kossert *et al.*, Eur. Phys. J. A **19**, 391 (2004).
[49] H. Herminghaus *et al.*, IEEE Trans. Nucl. Sci. **30**, 3274 (1983).
[50] T. Walcher, Prog. Part. Nucl. Phys. **24**, 189 (1990).
[51] K.-H. Kaiser *et al.*, Nucl. Instrum. Methods Phys. Res., Sect. A **593**, 159 (2008).
[52] I. Anthony *et al.*, Nucl. Instrum. Methods Phys. Res., Sect. A **301**, 230 (1991).
[53] S. J. Hall, G. J. Miller, R. Beck, and P. Jennewein, Nucl. Instrum. Methods Phys. Res., Sect. A **368**, 698 (1996).
[54] J. C. McGeorge *et al.*, Eur. Phys. J. A **37**, 129 (2008).
[55] M. Dieterle *et al.*, Eur. Phys. J. A **51**, 142 (2015).
[56] M. Oberle *et al.*, Eur. Phys. J. A **50**, 54 (2014).
[57] D. Werthmüller *et al.*, Phys. Rev. C **90**, 015205 (2014).
[58] A. Käser *et al.*, Eur. Phys. J. A **52**, 271 (2016).
[59] M. Oberle *et al.*, Phys. Lett. B **721**, 237 (2013).
[60] S. Schumann *et al.*, Eur. Phys. J. A **43**, 269 (2010).
[61] F. Zehr *et al.*, Eur. Phys. J. A **48**, 98 (2012).
[62] A. Starostin, B. M. K. Nefkens, E. Berger, M. Clajus, A. Marusic, S. McDonald, N. Phaisangittisakul, S. Prakhov, J. W. Price, M. Pulver *et al.*, Phys. Rev. C **64**, 055205 (2001).
[63] R. Novotny, IEEE Trans. Nucl. Sci. **38**, 379 (1991).
[64] A. R. Gabler *et al.*, Nucl. Instrum. Methods Phys. Res., Sect. A **346**, 168 (1994).
[65] D. Watts, in *Calorimetry in Particle Physics, Proceedings of the 11th Internatinal Conference, Perugia, Italy 2004*, edited by C. Cecchi, P. Cenci, P. Lubrano, and M. Pepe (World Scientific, Singapore, 2005), p. 560.
[66] D. Werthmüller *et al.*, Phys. Rev. Lett. **111**, 232001 (2013).
[67] A. Käser *et al.*, Phys. Lett. B **748**, 244 (2015).
[68] L. Witthauer *et al.*, Eur. Phys. J. A **49**, 154 (2013).
[69] S. Agostinelli *et al.*, Nucl. Instrum. Methods Phys. Res., Sect. A **506**, 250 (2003).
[70] J. Apostolakis, D. H. Wright *et al.*, in *Hadronic Shower Simulation Workshop, Batavia, IL, 2006*, edited by M. Albrow and R. Raja, AIP Conf. Proc. No. 896 (AIP, New York, 2007), p. 11.
[71] I. Fröhlich *et al.*, J. Phys. Conf. Ser. **219**, 032039 (2010).
[72] M. Lacombe *et al.*, Phys. Lett. B **101**, 139 (1981).
[73] C. Patrignani *et al.*, Chin. Phys. C **40**, 100001 (2016).
[74] L. Witthauer *et al.*, Phys. Rev. Lett. **117**, 132502 (2016).
[75] L. Witthauer *et al.*, Phys. Rev. C **95**, 055201 (2017).
[76] L. Witthauer *et al.*, Eur. Phys. J. A **53**, 58 (2017).
[77] V. E. Tarasov *et al.*, Phys. At. Nucl. **79**, 216 (2016).
[78] S. X. Nakamura, H. Kamano, T.-S. H. Lee, and T. Sato, arXiv:1804.04757.
[79] A. V. Anisovich *et al.*, Eur. Phys. J. A **49**, 67 (2013).
[80] MAID [http://www.maid.kph.uni-mainz.de], SAID [http://www.gwdac.phys.gwu.edu], and BnGa [http://www.pwa.hiskp.uni-bonn.de]